Variability and accuracy of Zenith Total Delay over the East African tropical region

Ssenyunzi, Richard Cliffe; Oruru, Bosco; D'ujanga, Florence Mutonyi; Realini, Eugenio; Barindelli, Stefano; Tagliaferro, Giulio; van de Giesen, Nick

DOI
10.1016/j.asr.2019.05.027

Publication date
2019

Document Version
Final published version

Published in
Advances in Space Research

Citation (APA)
Ssenyunzi, R. C., Oruru, B., D'ujanga, F. M., Realini, E., Barindelli, S., Tagliaferro, G., & van de Giesen, N. (2019). Variability and accuracy of Zenith Total Delay over the East African tropical region. *Advances in Space Research*, *64*(4), 900-920. https://doi.org/10.1016/j.asr.2019.05.027

Available online at www.sciencedirect.com

ScienceDirect

Advances in Space Research 64 (2019) 900–920

ADVANCES IN SPACE RESEARCH (a COSPAR publication)

www.elsevier.com/locate/asr

Variability and accuracy of Zenith Total Delay over the East African tropical region

Richard Cliffe Ssenyunzi [a,b,*], Bosco Oruru [a], Florence Mutonyi D'ujanga [a], Eugenio Realini [c], Stefano Barindelli [d], Giulio Tagliaferro [c], Nick van de Giesen [e]

[a] Department of Physics, Makerere University, P.O. Box 7062, Kampala, Uganda
[b] Department of Physics, Busitema University, P.O. Box 236, Tororo, Uganda
[c] Geomatics Research & Development srl, Via Cavour 2, 22074 Lomazzo, Italy
[d] Department of Civil and Environmental Engineering, Politecnico di Milano, P.zza Leonardo da Vinci 32, 20133 Milano, Italy
[e] Water Management, Civil Engineering and Geosciences TU Delft, P.O. Box 5048, 2600 GA Delft, The Netherlands

Received 13 August 2018; received in revised form 5 May 2019; accepted 15 May 2019
Available online 4 June 2019

Abstract

The Global Navigation Satellite System (GNSS) can be used to derive accurately the Zenith Tropospheric Delay (ZTD) under all-weather conditions. The derived ZTDs play a vital role in climate studies, weather forecasting and are operationally assimilated into numerical weather prediction models. In this study, variations and statistical analysis of GNSS-derived ZTD over the East African tropical region are analysed. The data is collected from 13 geodetic permanent stations for the period of 4 years from 2013 to 2016. The 13 stations consist of 5 International GNSS Service (IGS) stations plus 8 stations as follows: 4 Africa Array stations and 4 Malawi Rifting stations from Uganda, Kenya, Tanzania and Rwanda. The ZTD time series were processed using goGPS software version 1.0 beta1, a MATLAB based GNSS processing software, originally developed for kinematic applications but recently re-engineered for quasi static applications. The annual variation of the ZTD time series was investigated using Lomb Scargle periodograms. The semi-annual frequency has the dominant power in subregion 1 (latitudes 4 °S and 4 °N) and the annual frequency has the dominant power in subregion 2 (latitudes 12 °S to 4 °S). The highest ZTD estimates occur during the rainy seasons, at all stations, and the lowest estimates occur during the dry seasons. The results also show that the ZTD estimates are largest at stations located at low elevation (regions close to the Indian Ocean). The derived ZTDs are compared to the values derived from the GIPSY-OASIS via Jet Propulsion Laboratory (JPL) online Automatic Precise Positioning Service (APPS) and the Unified Environmental Modelling System (UEMS) numerical weather prediction (NWP) model. The comparison of goGPS and APPS ZTD at the 13 stations shows an overall average bias, Root Mean Square (RMS) and standard deviation (stdev) of −0.9 mm, 3.2 mm and 3.0 mm respectively, with correlation coefficients ranging from 0.974 to 0.999. The comparison of goGPS ZTD against UEMS NWP ZTD at 8 selected stations shows average bias, RMS and stdev of −12.4 mm, 22.0 mm and 17.6 mm respectively, with correlation coefficients ranging from 0.802 to 0.974. The agreement between the GPS ZTD and the NWP ZTD indicates that goGPS ZTD can be assimilated into NWP models in the East African region.

Keywords: Precise point positioning; Zenith tropospheric delay; GNSS; goGPS; UEMS-NWP

1. Introduction

The troposphere is the lowest part of neutral atmosphere which acts mainly as a medium of energy transfer and as a host to meteorological (weather) phenomena. It extends

* Corresponding author at: Department of Physics, Makerere University, P.O. Box 7062, Kampala, Uganda.
E-mail address: ssecliffe@gmail.com (R.C. Ssenyunzi).

https://doi.org/10.1016/j.asr.2019.05.027
0273-1177/

from the earth's surface up to an altitude of approximately 16 km at the Equator and 9 km at the poles (Dodo and Idowu, 2010). The Earth's troposphere, with its lower boundary on the Earths surface, is composed of about 75–80% of the total molecular mass of the atmosphere and almost all the water vapour and aerosols (Schuler, 2001; Hackman et al., 2015). The troposphere, according to its composition, consists of the dry (or hydrostatic) and wet components (Saastamoinen, 1972). The dry component mainly consists of the atmospheric dry air gases such as nitrogen, oxygen, argon and other constituents which account for about 99% of the total volume. The wet component is mainly composed of water vapour (Davis et al., 1985). The main source of water vapour is the evaporation from water bodies and transpiration by plants. The water vapour content depends on the local geographic conditions and meteorological phenomena. Its concentration is at most 1% of the volume of the air in the polar and desert regions and constitutes over 4% of the volume of the air in the tropics. Therefore, water vapour in the troposphere features large spatial and temporal variations.

When the GNSS signals travel in the atmosphere from the satellites to the ground-based receivers on Earth, they are affected by several processes. These include, reflection and refraction processes due to dry air, water vapour, hydrometeors (particularly the liquid content of the clouds and heavy rainfall) and other particles such as sand, dust, aerosols, and volcanic ash in the troposphere (Solheim et al., 1999; Adegoke and Onasanya, 2008). This leads to a change in the signal's velocity, thereby affecting the GNSS positioning accuracy (Musa et al., 2011; Yao et al., 2016). The delays or errors induced on GNSS signals during their propagation through the atmosphere are referred to as ionospheric and tropospheric delays (Kurekar and Kuraishi, 2012). Ionospheric delay is caused by the presence of free electrons in the ionosphere which is the ionized portion of the upper atmosphere. The ionospheric delay is dispersive in nature and depends on the frequency of the signal (Bhattacharya et al., 2008). It can be eliminated by the use of a linear combination of two or multiple frequencies since the GNSS broadcasts at two or more separate frequencies. Unlike the ionospheric delay, the delay due to the neutral part of the atmosphere does not depend on signal frequencies (Younes, 2016). It is mostly caused by the troposphere and is referred to as the tropospheric delay. The tropospheric delay consists of the dry or hydrostatic and wet components. The wet component which is normally the largest source of inconsistency in the atmospheric delay, depends on the content of water vapour in the troposphere (Jin et al., 2007; Valadez et al., 2007). Therefore, this study will focus on the tropospheric delay since it has turned out to be a very important source of information on atmospheric water content that is a vital ingredient in meteorology applications and climate studies (Notarpietro et al., 2012). The total delay path mapped onto the zenith direction is referred to as the Zenith Tropospheric (or Total) Delay.

Several studies have demonstrated the use of GNSS in estimation of the ZTD e.g. (Emardson et al., 1998; Vedel et al., 2001; Jin and Park, 2005; Jin et al., 2007). Emardson et al. (1998) and Jin et al. (2007) discovered that GNSS-derived ZTD has high temporal resolution compared to other techniques such as radiosondes. Also Teke et al. (2011) found out that GNSS-estimated ZTDs are accurate and consistent with other observational systems such as very long baseline interferometry and radiosondes. Using data from global GNSS, Jin et al. (2007, 2009) analysed the diurnal and semi-diurnal components of ZTD through harmonic functions, confirming the presence of seasonal ZTD cycles. It was also observed that the temporal and spatial characteristics of climatic weather and its processes can be described well by ZTD since it is an essential atmospheric parameter.

The derivation of ZTD has been successfully achieved through the use of mapping functions e.g (Saastamoinen, 1972; Davis et al., 1985; Baby et al., 1988; Niell, 1996, 2000). The ZTD can be computed by the integration of refractivity (N) along the signal path through the neutral atmosphere a follows.

$$ZTD = c\tau = 10^{-6}\int_{ha}^{\infty} N(h)\cdot dh \tag{1}$$

where c and τ are the speed of light in vacuum, and the delay measured in units of time respectively, ha is the GPS antenna height. The signal refractivity of the neutral atmosphere is a function of pressure, temperature, water vapour pressure (Davis et al., 1985; Hadas et al., 2013) and can be expressed as follows.

$$N = k_1\cdot\left(\frac{P_d}{T}\right)\cdot Z_h^{-1} + \left(k_2\cdot\frac{e}{T} + k_3\cdot\frac{e}{T^2}\right)\cdot Z_w^{-1} \tag{2}$$

where P_d and e are the partial pressure (in hPa) of dry gases and water vapour (respectively), T is the air temperature (in K), $k_1 = (77.6848 \pm 0.0094)$ K hPa^{-1}, $k_2 = (71.2152 \pm 1.3)$ K hPa^{-1} and $k_3 = (375463 \pm 0.76)$ K^2 hPa^{-1} are refractivity constants (Rueger, 2002). $Z_h^{-1} \approx Z_w^{-1} \approx 1$ are inverse compressibility factors for dry gas and water vapour (respectively). The atmospheric refractivity can be expressed as a sum of a hydrostatic and wet refractivity

$$N = N_{hyd} + N_{wet} = k_1\cdot R_d\cdot\rho + \left(k_2'\cdot\frac{e}{T} + k_3\cdot\frac{e}{T^2}\right) \tag{3}$$

where $k_2' = k_1 - k_2\cdot\frac{M_w}{M_d}$, M_w and M_d are molar weights of water vapour and dry air respectively. R_d and ρ are the gas constant of dry air and total density of air respectively. The total zenith path delay is, therefore, expressed as,

$$ZTD = 10^{-6}\int_{h}^{\infty}(k_1\cdot R_d)\cdot dh + 10^{-6} \times \int_{h}^{\infty}\left(k_2'\cdot\frac{e}{T} + k_3\cdot\frac{e}{T^2}\right)\cdot dh \tag{4}$$

where dh is differential change in height. Assuming the atmosphere to be in hydrostatic equilibrium, the vertical coordinate can be transformed from height to pressure. It can be shown that ZTD can be expressed as,

$$ZTD = -10^{-6}\int_{pa}^{0} k_1 \cdot R_d \cdot \frac{1}{g} \cdot dp + -10^{-6}\int_{pa}^{0} \frac{1}{\rho \cdot g} \cdot \left(k_2' + \frac{k_3}{T}\right) \cdot \frac{e}{T} \cdot dp \quad (5)$$

where $pa$is the atmospheric pressure at GPS antenna height, pressure at infinity is taken to be zero and $dp = -\rho \cdot g \cdot dh$. Therefore, ZTD is a function of the Zenith Hydrostatic Delay (ZHD) and the Zenith Wet Delay (ZWD) (Guerova et al., 2016).

$$ZTD = ZHD + ZWD \quad (6)$$

The ZHD can be adequately modeled from surface pressure or using pressure data from models (Numerical weather models or alternatively, empirical meteorological models). The ZWD is either directly reported or computed as unknown parameter by subtracting ZHD from ZTD (Klos et al., 2018). At GNSS frequencies, tropospheric delay can be over 2 m at the zenith and over 20 m at the lower elevation angles (Kouba, 2009; Yao et al., 2016).

The estimation of ZTD from GNSS observations can be obtained from at least two data processing modes: Precise Point Positioning (PPP) and network mode. In the PPP mode, the data are processed at each station independently, and this involves the application of precise satellite orbits and clocks in the processing. This processing mode is very efficient and can be performed for any number of stations (Aigong et al., 2013). In the network mode, the observations from a number of stations are processed together. With this mode, most observation errors can be cancelled by forming differential observations between stations.

There is an increasing use of PPP for processing the GNSS data using different software packages that have been developed (Astudillo et al., 2018). However, the main problem of using the PPP method is the long interval of about 20–30 min required for the solution convergence (Dousa and Vaclavovic, 2014; Wonnacott and Merry, 2006). This is due to the high correlation among the estimated parameters which include the troposphere delay, receiver clock offset and receiver height. However this can be overcome when a high-quality troposphere delay model is applied to constrain the troposphere estimates (Hadas et al., 2013; Wonnacott and Merry, 2006). In this study, a network of 13 GNSS stations equipped with dual-frequency receivers were used and data from each station were processed independently in the PPP mode to estimate ZTD.

The East African tropical region is part of the African Equatorial region with the equator passing through two of its countries (Uganda and Kenya). The equatorial atmosphere holds more water vapour than any other region on the earth, characterised by short periodic variations (Musa et al., 2011). Since the large amount of water vapour is found in the equatorial regions, a better understanding of tropospheric effect on GNSS positioning accuracy is needed. However, East African region faces more challenges due to its terrain heterogeneities and variable topography, insufficient and inconsistent data, lack of ground-based tropospheric monitoring instruments and a scattered network of GNSS reference sites. The inconsistency of data streaming from the various stations in Africa is mainly due to communication problems, caused by poor internet connectivity, equipment failure, or in some cases electrical power problems, although this happens less often (Isioye et al., 2015a). Due to these factors, the efforts are rather recent in terms of tropospheric delay studies in this region.

Several studies on deriving ZTD measurements from ground-based GPS measurements have been carried out in Africa e.g. (Abdelfatah et al., 2009; Dodo and Idowu, 2010; Mousa, 2012; Abdelfatah et al., 2015; Isioye et al., 2015a,b, 2018). However, data from the East African tropical region have not yet been much documented. This, therefore, calls for an in-depth study of ZTD variation in the East African tropical region to refiner earlier studies such as Isioye et al. (2015a) which used scattered GPS receiver stations. Also different regions show different behaviours of ZTD due to differences in season, latitude, surface altitude and wether the atmosphere is located above land or sea. Studies on estimation of GNSS-derived ZTD in Africa have been enabled due to the presence of the GPS ground receiver sites for geodetic studies for some regions such as those from African Monsoon Multidisciplinary Analysis (AMMA) project, 1999–2005 over West Africa (Walpersdorf et al., 2007; Bock and Nuret, 2009), the realization of the African Geodetic Reference Frame (AFREF), and South Africa's national network (TRIGNET) among others. These have initiated the investigation of ZTD or PWV over some of these regions such as (Wilgan et al., 2017; Bock et al., 2005, 2007; Koulali et al., 2011). The East African tropical region has also recently benefited from the Africa Array (AA) which has created a multidisciplinary research network for the broader Earth science community, by installing continuous Global Positioning System (CGPS) instruments fitted with meteorological (met) sensors (http://www.africaarray.psu.edu/) and the dense GNSS network for tectonics monitoring from Malawi.

The variation of ZTDs in some parts of Africa have been investigated in different studies. For instance, Isioye et al. (2015a), used sparse African GNSS network in the north, central and southern regions of the Africa. The results from zenith tropospheric delay (ZTD) from the African GNSS showed spatial variability and diurnal dependence of ZTD. Using estimates from GNSS data, Isioye et al. (2018) presented an in-depth analysis to comprehend the spatial and temporal variability of ZTD over Nigeria for a period of 5 years. It was observed that the diurnal ZTD cycles exhibited seasonal dependence, with

larger amplitudes in the rainy (wet) season and smaller ones in the dry season.

2. Data and methodology

2.1. Area of study

The area of study lies between the latitude range 12 °S to 4 °N and longitude range 28 °E to 44 °E, which is part of the East African tropical region. It covers Kenya, Rwanda, Tanzania, and Uganda, which are also part of the Great Lakes region, neighbouring the Indian Ocean (Fig. 1). The region is known to have a complex topography and a terrain that is defined by tropical rain forests, many inland Lakes such as Lake Victoria, the world's second largest freshwater Lake, Lake Tanganyika, the world's second deepest Lake and rift valleys. It is also defined by tall Mountains such as Mount Kilimanjaro and Mount Kenya, the two tallest peaks in Africa, and Mount Elgon among others (Fig. 2). These factors greatly influence the weather and the climate of this tropical region. Africa is divived into 15 homogeneous subregions based on observed Global Precipitation Climatology Centre (GPCC) rainfall data (Favre et al., 2011; Endris et al., 2013). The East African tropical region under study, shares 2 of the 15 subregions. For this study, the two subregions include subregion 1, between 4 °S and 4 °N, and subregion 2, between 12 °S and 4 °S, as shown in Fig. 1. Subregion 1 includes the following GNSS stations: MBAR (Uganda), MOIU (Kenya), RCMN (Kenya), MAL2 (Kenya), NURK (Rwanda) and ARSH (Tanzania). This subregion is characterized by a bimodal annual rainfall distribution with the major rainfall season in March to May and a shorter rainfall season in October to November/December and is the closest to the Equator. Subregion 2 includes the following GNSS stations: DODM (Tanzania), MTDK (Tanzania), MBEY (Tanzania), KFNY (Tanzania), SNGC (Tanzania), TNDC (Tanzania) and MTVE (Tanzania). This subregion is characterized by annual unimodal rainfall distribution spanning from November to April (Favre et al., 2011). This seasonal cycle is strongly created by north–south movement of the intertropical convergence zone (ITCZ) across the region in those months (Anyah et al., 2006). However the mountainous nature of some parts of East Africa may cause many changes from this general pattern. Rainfall variability in East Africa is generally high and the arrivals of the rainy seasons differ from year to year (Mutai et al., 1998). Temperatures in East Africa, except on the hot and generally humid coastal belt, are moderate, with maximum of over 30 °C and minimum of less than 15 °C at an altitude of 1,500 metres. At altitudes of above 2,500 metres, frosts are common during the dry season and maximum temperatures are typically about 21 °C or less. The atmosphere in this region is unique because it is located near the Equator and exposed to the Indian Ocean.

2.2. GNSS data

This study used GNSS data for a period of more than 3 years, with most sites observations from year 2013 to

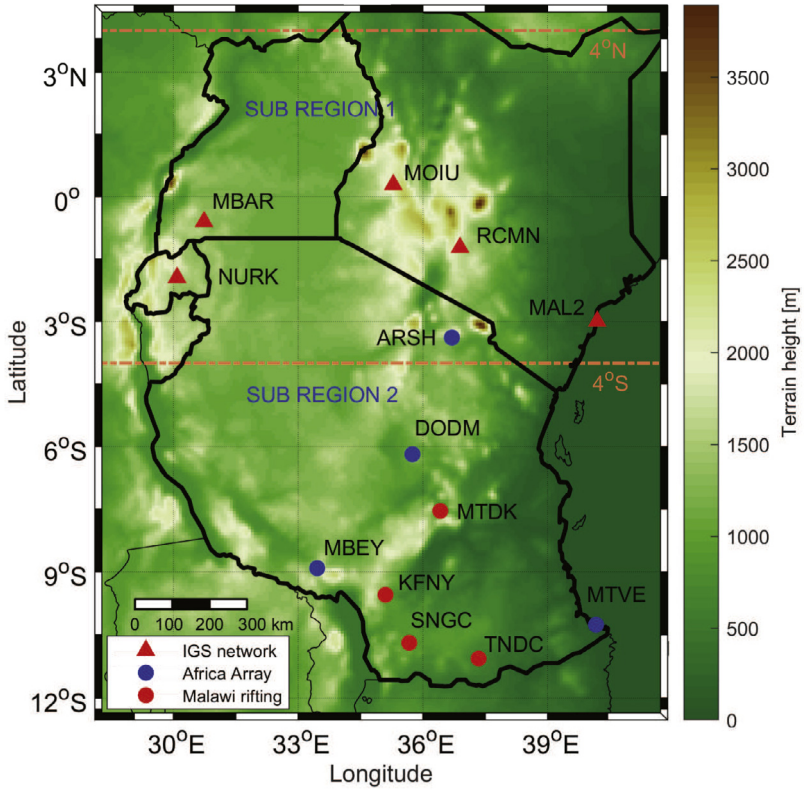

Fig. 1. Topography of the study area and distribution of the GPS stations in East African tropical region.

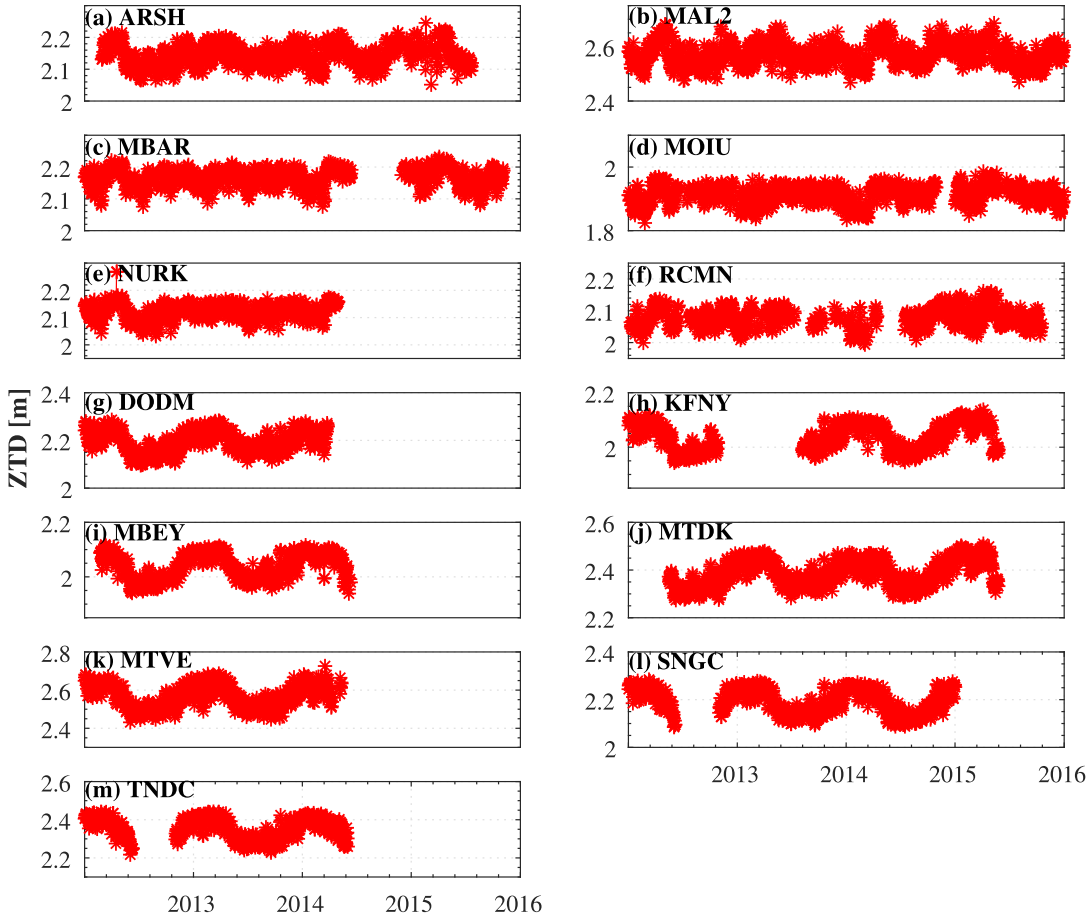

Fig. 2. Time series of GNSS ZTD (a)–(f) for subregion 1 and (g)–(m) for subregion 2.

2015. A number of 13 stations, one in Uganda, three in Kenya, one in Rwanda and eight in Tanzania were selected. Fig. 1 and Table 1 show the geographical locations of the selected GNSS stations from which data are used to obtain ZTD. All the stations are equipped with dual-frequency receivers; some have an observation recording rate of 15 s and others 30 s. The GNSS data was processed to obtain ZTD using two processing software packages: goGPS v1.0 beta1 and GIPSY-OASIS via Jet Propulsion Laboratory (JPL) online Automatic Precise Positioning Service (APPS). Table 2 presents processing options for both goGPS and online APPS to estimate the ZTD.

The Automatic Precise Positioning Service (APPS) is an online service provided by the Jet Propulsion Lab (http://apps.gdgps.net/) which can estimate position coordinates as a single set in Static Mode or a time series in Kinematic Mode using the GIPSY-OASIS software. APPS processes

Table 1
GNSS stations coordinates.

Staion Id and City	Country	Longitude (E) degrees	Latitude (N) degrees	Ellipsoidal height (m)	Available data
RCMN (Nairobi)	Kenya	36.8935	−1.2210	1591.9667	2013–2016
MAL2 (Malindi)	Kenya	40.1941	−2.9960	−20.9371	2013–2016
MOIU (Eldoret)	Kenya	35.2900	0.2883	2201.5109	2013–2016
NURK (Kigali)	Rwanda	30.0897	−1.9446	1483.8088	2013–2015
MBAR (Mbarara)	Uganda	30.7379	−0.6015	1337.5297	2013–2016
MBEY (Mbeya)	Tanzania	33.4592	−8.9118	1700.5135	2013–2015
ARSH (Arusha)	Tanzania	36.6984	−3.3869	1345.1606	2013–2016
DODM (Dodoma)	Tanzania	35.7482	−6.1865	1122.5948	2013–2015
SNGC (Songea)	Tanzania	35.6728	−10.6898	1181.2205	2013–2015
TNDC (Tunduru)	Tanzania	37.3405	−11.0626	672.9480	2013–2015
MTVE (Mtwara)	Tanzania	40.1656	−10.2599	−11.4143	2013–2015
MTDK(Mtandika)	Tanzania	36.4206	−7.5440	548.1747	2013–2016
KFNY (Kifanya)	Tanzania	35.1025	−9.5468	1714.8343	2013–2016

Table 2
GNSS data processing options.

Processing method	APPS	goGPS
Approach strategy	PPP	PPP
Sampling interval (s)	300	30
Frequency observed	L1 + L2	L1 + L2
Orbits and clocks of satellite	JPL final	IGS Final (.sp3) IGS final (.clk)
Frame of reference	ITRF2008	ITRF2008
Satellite/receiver PCV	IGS08.atx	IGS08.atx
Ocean loading	default	FES2004
Ionospheric model	Ionospheric-free combination	Ionospheric-free combination
Cut-off elevation	10 degrees	10 degrees
Mapping functions	GMF	VMF
Type of observation	Code and phase	Code and phase
Version	GIPSY 6.4	1.0 beta1

only dual-frequency GPS observations and allows the user to use Final, Rapid and Ultra-rapid type products by the JPL for correcting satellite orbits and clocks. The ZTD is estimated by applying the Global Mapping Function (GMF) (Böhm et al., 2006).

The estimate of ZTD also involved the use of goGPS software. goGPS is a MATLAB based GNSS processing software (Realini and Reguzzoni, 2013; Herrera et al., 2016), originally developed for kinematic applications, it has recently re-engineered to fit quasi static applications. In PPP mode (Zumberge et al., 1997) it can be used to estimate ZTD parameters for meteorological applications (Barindelli et al., 2018; Krietemeyer et al., 2018). goGPS applies corrections for antenna phase wind up, relativistic effects, GNSS antennas phase center offset and variations, Earth tide, polar motion earth tides, and ocean Tide Loading (OTL) effects by using coefficients obtained from (http://holt.oso.chalmers.se/loading) using FES 2004 model. The wet components of the delay is estimated as an unknown together with its north and east gradients, the receiver clock offset, the station position and the carrier phase ambiguities using a least squares adjustment with observations coming from one day of data. The temporal resolution of ZTD estimates from goGPS is 30 s, the variation of the ZTD is regularized in a Tykhonov sense with a standard deviation of $0.03\ \mathrm{m}/\sqrt{\mathrm{h}}$. The used mapping function is the Vienna Mapping Function (VMF). Continued fraction form coefficient for the VMF as well as hydrostatic delays are spatially interpolated from gridded data obtained from (http://ggosatm.hg.tuwien.ac.at/DELAY/GRID/VMFG/) following the procedure described in Kouba (2008). The PPP method (Zumberge et al., 1997) applied in this study relies on highly accurate satellite orbits and clocks provided by the International GNSS Service (IGS) (Kouba, 2009).

2.3. Numerical weather model

In this study we used data from the Unified Environmental Modeling System (UEMS), previously known as the Weather Research and Forecasting Environmental Modeling System (WRF-EMS). UEMS is a complete, full-physics, Numerical Weather Prediction (NWP) package that incorporates dynamical cores from both the National Center for Atmospheric Research (NCAR) Advanced Research WRF (ARW) and the National Center for Environmental Predictions' (NCEP) Non-hydrostatic Mesoscale Model (NMM) models into a single end-to-end forecasting system. The UEMS NWP model was set to a computational domain that extends from approximately 28 °E to 42 °E in longitude and approximately 4 °N to 12 °S in latitude. The horizontal dimension consists of 193 by 241 grid points in x- and y-axis respectively with a grid spacing of 8 km. The vertical dimension consists of 45 vertical levels. The Mercator map projection type was used and ARW model as the WRF dynamical core for the simulation. The Kessler and Kain-Fritsch schemes were used for microphysics and cumulus parameterization respectively. Initialization was done by use of the 6 hourly Global Forecast System (GFS) 0.5 degree global model. Simulations were made for each day from June 2015 to May 2016, with each simulation having a forecast length of 24 h. This resulted into 25 hourly NetCDF output files for each simulation.

The next step involves retrieval of required variables from NWP model output files. In this step, the GNSS reference site is identified in terms of its longitude and latitude coordinates and a pair of indices corresponding to the latitude and longitude variables are then extracted from the NetCDF files. Four nearest neighboring grid points are then identified. This gives a 2-dimensional plane with the point of interest at the center and a grid point at each of the four corners. At these grid points we find all the required variables. Longitude and latitude variables at each of these four grid points are extracted and then used to extract a target variable at each of the four grid points. At this stage, we have a series of 2-dimensional planes extending vertically at each of the model half mass levels. By use of the longitude and latitude variables at the point of interest and at the four nearest neighboring grid points, the target variable is bilinearly interpolated to the point of

interest. Now we have the target variable not only at the four nearest neighboring grid points but also at the point of interest on each of the 2-dimensional planes. Finally, given that each half mass level is characterized by a given geometric height, we can linearly interpolate the target variable to the geometric height of the antenna at the GNSS site.

In a situation where the antenna is below model orography basic target variables are estimated by use of near surface variables and the standard atmosphere model. In order to determine variables at the antenna height, extrapolation of model level variables above the antenna may be performed if the antenna height is below the model surface. In such a case, the variables at the antenna height are estimated from the standard atmosphere model:

$$P_{ant} = P_{msl}(1 - 0.0000226ha)^{5.225} \tag{7}$$

$$T_{ant} = T_{msl} - 0.0065ha \tag{8}$$

where P_{ant} and T_{ant} are antenna height pressure (in hPa) and temperature respectively, ha is the antenna height, P_{msl} and P_{msl} are mean sea level pressure and temperature respectively.

In this work, the standard pressure and temperature models were preferred over the extrapolation procedures because they avoid errors associated with extrapolation of vertical model gradients that may be noisy. In case the antenna is within the model orography, vertical linear interpolation of the variables to the antenna height is performed to estimate variables at the antenna height. In estimation of ZTD, the target variables are pressure, temperature and water vapour mixing ratio. Other variables, for instance, local gravity acceleration at a point of measurement have to be derived. All the variables are directly extracted from the NWP output files as discussed below.

The water vapour mixing ratio is readily available at all the model levels. However, pressure and temperature variables have to be computed from other variables. The model output files contain base state pressure and perturbation pressure. The base state pressure is the mean value of pressure and a departure from this mean is the perturbation pressure. Pressure is therefore computed as a sum of these two pressure variables that are directly extracted from model half mass levels. Thus,

$$P = P_b + P_p \tag{9}$$

where P_b and P_p are the base state and perturbation pressure respectively.

The temperature variable contained in the model output is the perturbation potential temperature from 300 K. Potential temperature (in Kelvin) is, therefore, computed from,

$$\Theta = \theta + 300 \tag{10}$$

where Θ and θ are the potential and perturbation potential temperatures respectively. The absolute temperature is then computed using Poisson's equation for potential temperature as,

$$T = \Theta \cdot \left(\frac{P}{P_o}\right)^{\kappa} \tag{11}$$

where P is pressure determined in Eq. (9), P_o is the standard pressure. $\kappa = \frac{R_d}{C_p}$, where C_p is the specific heat capacity at constant pressure.

The geopotential heights at half levels are then converted to the corresponding geometric heights for computation of gravity acceleration. The geometric height at the j^{th} half level can be computed from,

$$h_j = \frac{H_j \cdot R_e}{G \cdot R_e - H_j} \tag{12}$$

where h_j is the geometric height (in km) at half mass level j, H_j is the geopotential height (in km) corresponding to h_j and R_e is the radius of the earth (in km) at latitude ϕ, given by, $R_e = \left(\frac{cos^2\phi}{R_{max}^2} + \frac{sin^2\phi}{R_{min}^2}\right)^{\frac{1}{2}}$. $G = \frac{g(\phi,h)}{g_o}$, where $g(\phi,h)$ is gravity at the point of measurement and g_o is the standard gravity at mean sea level (9.80665 ms^{-2}).

Given that the model extends to a vertical height of approximately 20 km some portion of the upper atmosphere is not covered by the model orography. Also a portion of the lower atmosphere is not covered by the model orography. This calls for caution in computing troposphere delays in both scenarios so that the method used tries to account for the delays due to the portions of the atmosphere not covered by the model orography. In formulating troposphere delays using NWP model variables, reference is made to the following formulations of ZHD and ZWD Eq. (5).

The ZTD value at a given station was therefore obtained by summing up the delay contributions from the Zenith Hydrostatic Delay (ZHD) and the Zenith Wet Delay (ZWD) as shown in Eq. (13).

$$ZTD_{NWP} = ZHD_{NWP} + ZWD_{NWP} \tag{13}$$

where

$$ZHD_{NWP} \approx ZHD_{upper} + ZHD_{within} + ZHD_{lower} \tag{14}$$

$$\approx 10^{-6} \cdot k_1 \cdot R_d \cdot \frac{1}{g_1} \cdot p_1 + 10^{-6} \cdot k_1 . R_d \cdot \frac{1}{g_1} \cdot \sum_{j=1}^{m} \frac{1}{g_j} \cdot \Delta P^h + 10^{-6} \cdot k_1 \cdot R_d \cdot \frac{1}{g_a} \cdot (p_a - p_j^h) \tag{15}$$

$$ZWD_{NWP} \approx ZWD_{upper} + ZWD_{within} + ZWD_{lower} \tag{16}$$

$$\begin{aligned} &\approx 10^{-6} \cdot \tfrac{R}{M_w} \cdot \tfrac{1}{g_1} \cdot (k_1 - k_2 \cdot \varepsilon + \tfrac{k_3}{T_1}) \cdot \tfrac{r_1}{r_1+1} \cdot p_1 \\ &+10^{-6} \cdot \tfrac{R}{M_w} \cdot \sum_{j=1}^{m} \cdot \tfrac{1}{g_j} \cdot (k_2 - k_1 \cdot \varepsilon + \tfrac{k_3}{T_j}) \cdot \tfrac{r_j}{r_j+1} \cdot \Delta p^h \\ &+10^{-6} \cdot \tfrac{R}{M_w} \cdot \tfrac{1}{g_a} \cdot (k_2 - k_1 \cdot \varepsilon + \tfrac{k_3}{T_a}) \cdot \tfrac{r_a}{r_a+1} \cdot (p_a - p_j^h) \end{aligned} \tag{17}$$

where p_1, T_1, r_1, g_1 and p_a, T_a, r_a, g_a are pressure, temperature, water vapour mixing ratio and local acceleration due to gravity at the topmost model level and at the GPS antenna height respectively. The g_j is the local acceleration due gravity at the j^{th} half level, $\Delta p^h = p^h_{j+1} - p^h_j$ is the difference in pressure at adjacent half levels $j+1$ and j respectively, m is the number of model half mass levels above the GPS antenna height, R_d is the universal gas constant for dry air, R is the universal gas constant, and $\varepsilon = \frac{M_w}{M_d}$ is the ratio of molar weight of water vapour to that of dry air.

Eqs. (15) and (17) are having three similar terms; the first term accounts for tropospheric delay above the model orography, the second term accounts for tropospheric delay within the model orography, and the third term accounts for tropospheric delay for a model layer bounded by the model level just above the GPS antenna and the actual antenna height. The portion of the atmosphere above the NWP model orography may contribute to the magnitude of the total delay though the value may be small and the overall effect of this portion differs from one NWP model to another. This depends on the maximum vertical extent of the model. For example for NCEP or NCAR models, the top (upper) level is 1 hPa, which corresponds to about 2 mm of ZHD according to Saastamoinen model, while for ERA-Interim, the top level pressure is only 0.1 hPa, corresponding to about 0.2 mm of ZHD, which is far below the GPS ZTD estimation errors (Lou et al., 2018). In the case of the ARW model which the UEMS applies, the pressure value at the top is a constant value of 50 hPa at a height of approximately 20 km. The vertical integration to estimate ZHD and ZWD is made up by the accumulation of each layer's contribution from the model lower level to the uppermost layer in the model (Brenot et al., 2006). However, according to Vedel et al. (2001), the ZHD outside the model cannot be neglected as it provides significant contributions up to an altitude of approximately 80 km.

3. Results and discussion

3.1. Variation of ZTD over the East Africa tropical region

The characteristics of ZTD over East African tropical region were analyzed using the time series of the measured ZTDs at 13 GNSS stations for 4 years from 2013 to 2016 see Fig. 2. The GNSS data were processed using the goGPS v1.0 beta1 software and the ZTDs were calculated at 1-hourly interval for each of the 13 stations. From Fig. 2, stations (a)–(f) are from subregion 1 and stations (g)–(m) are from subregion 2. The temporal variability in GNSS ZTD across the area of study is analysed: the two subregions considered exhibit distinct trends in GNSS ZTD variability. As observed in Fig. 2, stations in subregion 1 (near Equator) indicate that the time series of ZTDs didn't exhibit a clear expected annual signal described by the cosine function. This could be due to the small season cyles observed in water vapour in the African equatorial regions by Bock et al. (2007). The small season cycles could probably be due to the influence of the oceans and the lack of a Coriolis effect at the equator, and thus the fundamental dynamics of synoptic-scale systems in the tropics differ from those in other regions. The stations in subregion 2 indicate that the time series of ZTDs exhibit a strong well known annual signal, described by a cosine function (Song et al., 2011) with a periodical change of approximately 1-year cycle (Yao et al., 2016).

The oscillations in the ZTD time series were obtained using the Lomb-Scargle periodograms method in Figs. 3 and 4, as described in Glynn et al. (2006) and Zechmeister and Kurster (2009) for the 13 stations from East African tropical region. Because of gaps in the ZTD time series data (Fig. 2), it was not possible with other methods such as the Fast Fourier Transformation (FFT), hence the use of Lomb-Scargle periodograms. The Lomb-Scargle periodogram applied in this study, is used widely for the estimation of the power spectral density of incomplete or unevenly sampled time series for a given variable (Hocke and Kämpfer, 2008). This method estimates the frequency spectrum based on a least square fit of sine and cosine models of the observed time series (Lomb, 1976). It can be seen from the periodogram in Fig. 3 that for stations in subregion 1 with the exception of ARSH and MOIU, the semi-annual frequency has the dominant power followed by the annual frequency. The different results at ARSH and MOIU could probably be due to abnormalarities caused by abrupt changes in weather at the two sites.

Fig. 4 shows the periodogram for stations in subregion 2. It is observed that the annual frequency has the dominant power followed by very small semi-annual frequency at a few stations such as TNDC and SNGC. The strong annual signal may be caused by highest temperatures in summer and the lowest temperatures in winter which cause annual weather oscillation in this subregion. The different seasons considered for this subregion are the same to that applied in Southern Hemisphere (Jin et al., 2009). Generally, an examination of the plots as presented in Figs. 3 and 4 reveal that sites very close to the equator (subregion 1), the semi-annual signals are more dominant and all stations to the south of Equator (subregion 2), the annual signal dominates. Hence, the nature of the occurring oscillations of the ZTD reflects climate character in area of the station. Considering the stations between 12 °S to 4 °S (subregion 2) to belong to the southern Hemisphere (Camberlin, 2018), the results in this study agree well with other studies, e.g. Jin et al. (2009). Jin et al. (2009) observed that the semi-annual variation amplitudes of ZTD in the Southern Hemisphere are not significant and the amplitudes of annual ZTD variation are smaller at the equator areas.

Figs. 5 and 6 show 1-hourly averages of the ZTD displayed using box and whisker plots for the selected GNSS stations over East African tropical region from 2013 to 2016. The red horizontal line inside each box indicates

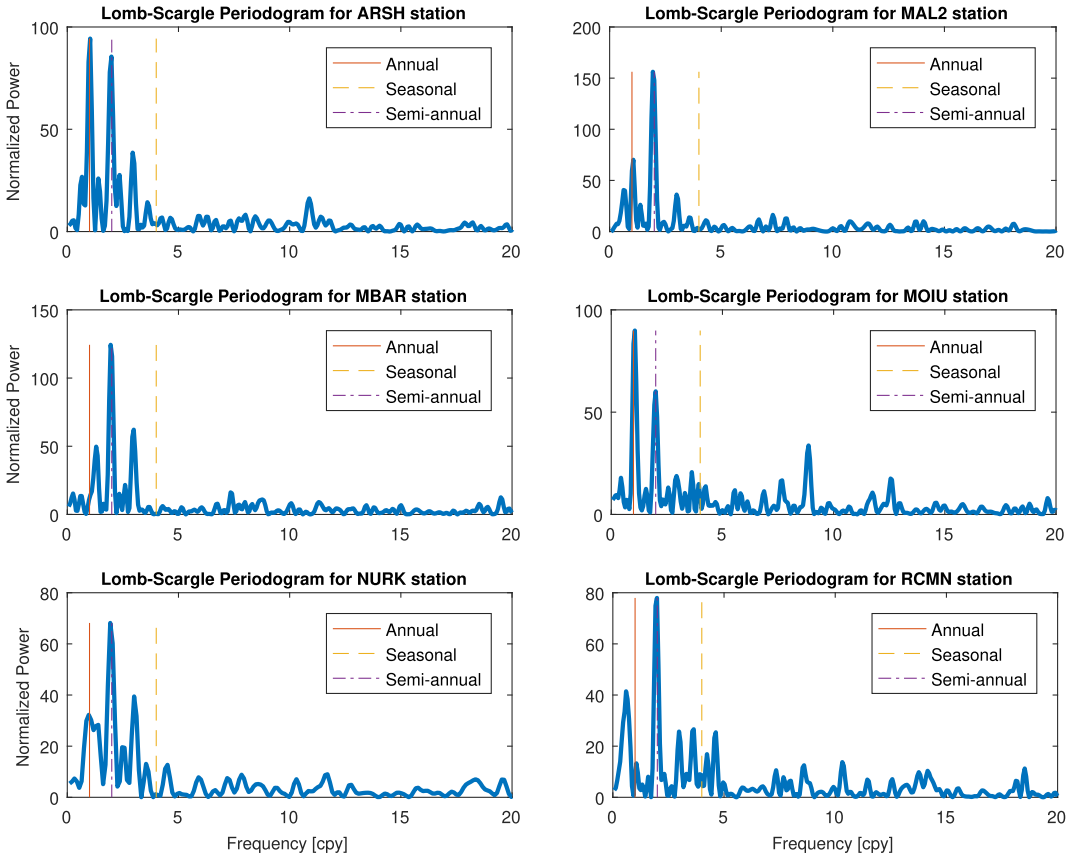

Fig. 3. Lomb-Scargle Periodogram of ZTD time series from stations in subregion 1.

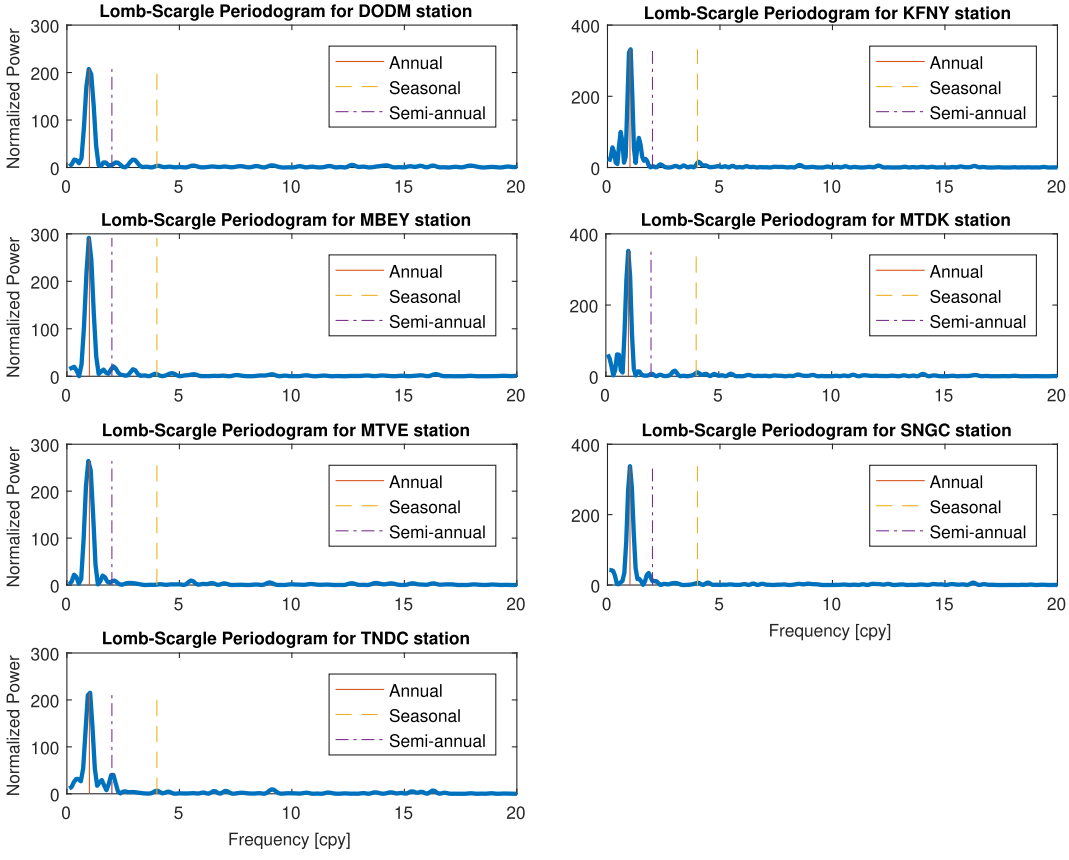

Fig. 4. Lomb-Scargle Periodogram of ZTD time series from stations in subregion 2.

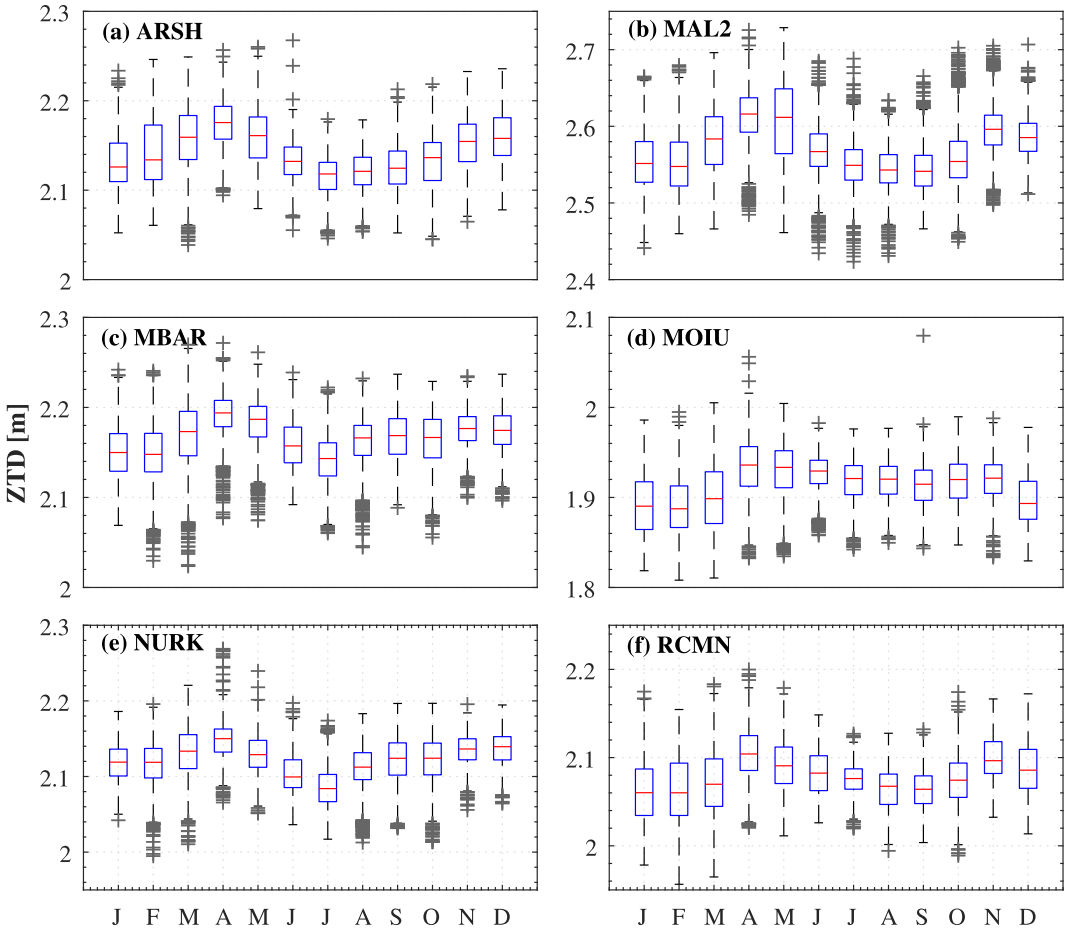

Fig. 5. Box and whisker plots of ZTD values over the time period from 2013 to 2016 for station in subregion 1.

the median value of the data, and the bottom and top lines of each box indicate the median value of the lower half and upper half of the data respectively. The horizontal lines at the bottom and top of vertical dashed line of each box indicate the minimum and maximum value of the data set respectively, whereas the extreme points marked by plus signs are outliers. Defining $Q1$ as the lower quartile (25th percentile), $Q3$ as the upper quartile (75th percentile) and $IQR = (Q3 - Q1)$ as the interquartile range, outliers are identified as values lower than $Q1 - 1.5IQR$ or higher than $Q3 + 1.5\ IQR$ (roughly corresponding to ± 2.7 sigma for normally distributed data). The figures clearly illustrate fluctuations in the datasets across the different months and stations. From Fig. 5, the median values of the ZTD indicate an increase from a minimum value in January to a maximum value in April at all stations and then a decrease to a minimum value between June and August. The median values of the ZTD then increase gradually to another maximum value in November. The maximum median value in April is however higher than that observed in November. According to Isioye et al. (2018), there is a strong correlation between precipitation and ZTD. April and November with high peaks of ZTD values are therefore associated with the peaks of the rainy seasons in this subregion. According to Camberlin (2018), areas around the equator and the Indian Ocean coastal plains are characterised by double-peak regimes with rains in the transition seasons in March-April-May (MAM) and October-November-December (OND). The MAM season is called the long rains and OND referred to as short rains season. This seasonal cycle in this subregion is strongly due to changes in the Hadley circulation with a twice a year migration of the Intertropical Convergence Zone (ITCZ) from south to north and backwards from north to south (Nicholson, 1996). This migration is accompanied by a change in the wind direction, moving from a northerly to a southerly direction in boreal winter and boreal summer respectively, demonstrating the nature of monsoons. The OND season receives low rainfall amount as compared to the MAM season due to the Western Indian Ocean sea-surface temperature (SST) being lower in OND. This results into a drier, more stable atmosphere (Yang et al., 2015) and an equatorial westerly flow from the western to the eastern Indian Ocean associated with moisture (Camberlin, 2018). The OND rains increase when easterlies are stronger, resulting in the eastern side being wetter than in MAM, where more rain is linked to westerly anomalies. The MAM and OND seasons are separated by two dry sea-

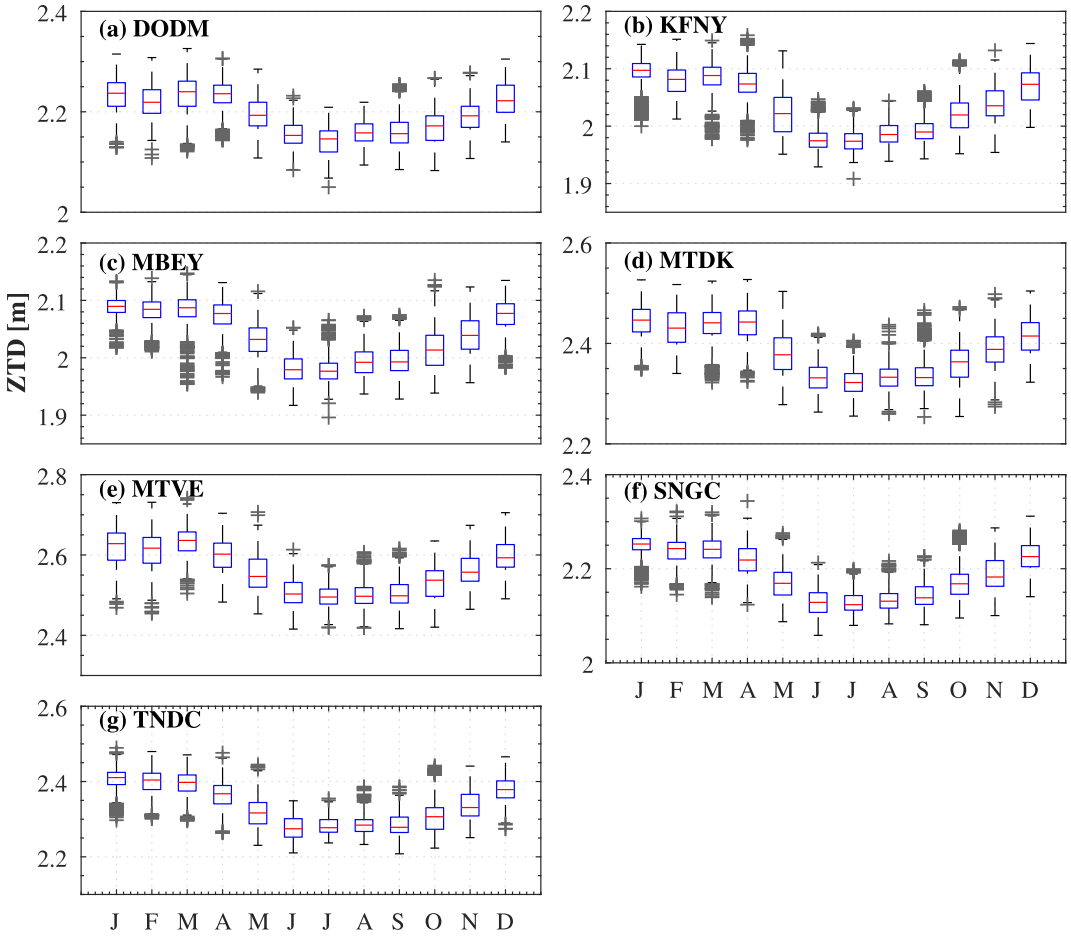

Fig. 6. Box and whisker plots of ZTD values over the time period from 2013 to 2016 for stations in subregion 2.

sons, of which the boreal summer between June and September is the longest and driest (Camberlin, 1997). The boreal summer dryness is caused by stable southeasterlies (Yang et al., 2015) and over a third of the rainfall maximum is found in this season due to the presence of mid-tropospheric moist westerlies and a low pressure anomaly (Davies et al., 1985). In this subregion, highest temperatures are experienced in February and March before the main rains, while lowest temperatures are experienced in July and August, during the relatively dry but cloudy season.

From Fig. 6, the median values of ZTD decrease gradually from the highest value in January to the lowest values in July–September, then gradually increases to a maximum value in December. The seasonal variability of ZTD in this subregion, has one observed peak in December–January. This subregion is characterized by unimodal rainfall distribution spanning from November to April. Also Camberlin (2018) reported that Southern Tanzania exhibits single peak regimes with a summer maximum corresponding to the ITCZ being located in the southern hemisphere and rainy season in this region is quite broad, with relatively heavy rainfall amounts from November to April.

Generally according to Camberlin (2018), the bimodal regimes (April and November) in the region under study prevail in the east, gradually shifting to a single austral summer peak to the south. The seasonal shift of the Intertropical Convergence Zone and its replacement in January-February and June-September by strong meridional, generally diverging low level winds, are responsible for the low rainfall. Figs. 5 and 6 have clearly exhibited fluctuations in the ZTD datasets across the different months and stations, with minima or maxima, describing the distinct seasons in East African tropical region: probably the rainy season and the dry season.

The results from this study are in good agreement with the previous study by Isioye et al. (2018). According to Isioye et al. (2018), ZTD follows a strong intra seasonal cycle, greatest in the wet season and least in the dry season, influenced by the saturation vapour pressure set by local temperatures and air masses. It was further observed that ZTDs reach very high amplitudes at the peak of the wet season, characterized by very high rainfall. This indicates that, in rainy seasons, the GNSS signal is delayed more by the troposphere as also reported by Isioye et al. (2018), possibly due to presence of large amounts of water

vapour. According to Abraha et al. (2015), rainfall is always dependent on the water vapour content though the presence of water vapour in the atmosphere does not mean that there will always be rainfall.

In this study, the average ZTD and ZWD for different seasons are analysed. The different seasons considered in this study include March-April-May (MAM), June-July-August (JJA), September-October-November (SON) and December-January-February (DJF). These represent the spring, summer, autumn and winter in the Northern Hemisphere and the autumn, winter, spring and summer in the Southern Hemisphere (Jin et al., 2009). To investigate the seasonal variation in detail, the average values of the goGPS ZTD for each month is determined and then an average of those values for all the months that constitute a particular season for each station is obtained. The results of each season are then displayed as shown in Table 3. From Table 3, the average values of ZTD at most GPS sites in subregion 1 are maximum in spring season (MAM) with average ZTD values ranging between 1.92 m and 2.60 m. The lowest average values in this subregion are observed during summer (JJA) with values ranging between 1.92 m and 2.55 m. The average values of ZTD at GPS sites in subregion 2 are maximum in summer (DJF) with average ZTD values ranging between 2.08 m and 2.61 m. The lowest average values in this region are observed during winter (JJA) with average values ranging between 1.98 m and 2.50 m. The stations within coastal sites (MTVE and MAL2), show the highest ZTD values (above 2.5 m) and this is probably influenced by the low elevation and the related high temperature, the humidity and the evapotranspiration cycle (Abraha et al., 2015).

The inconsistency in ZTD is largely due to variation in ZWD which is related to water vapour. To understand more of the seasonal variation of ZTD, seasonal variation in ZWD is also analyzed. Fig. 7 shows seasonal mean of ZWD from UEMS NWP model from June 2015 to May 2016 for the four seasons. It is observed from Fig. 7 that regions near Indian Ocean show the highest amount of ZWD/ZTD for all the four seasons, with ZWD values higher than 0.25 m. However, there is a consistent low ZWD (ZTD) region in all the four seasons, which is in the Kenya and probably in the region where MOIU station is located. This is probably related to the elevation of that region which is relatively high over 2000 m. This station is also shown in Fig. 5(d). This implies elevation also has some impact on ZWD or ZTD and higher elevation stations have lower ZWD (ZTD) such as MOIU at 2201.5 m and KFNY at 1714.8 m. For the two subregions considered as making up the East African tropical region in this study, larger ZWD (ZTD) values are observed during the spring (MAM) followed by autumn (SON) and lower values are observed during summer (JJA) for subregion 1. For subregion 2, larger ZWD (ZTD) values are observed during the summer (DJF) followed by autumn (MAM) and lower values are observed during winter (JJA). This study is in agreement with other studies such as Jin et al. (2007). According to Jin et al. (2007), the variation in ZTD on inter-annual and seasonal scales has a maximum value of ZTD in spring for the equatorial region (subregion 1) and in the austral summer for the southern polar region (subregion 2). The spring season in the equatorial region of Africa is seen as the wet season and is known as a period of high amplitude in ZTD cycles.

Table 3
Average station ZTD and seasonal mean.

Site	av.ZTD (m)	MAM (m)	JJA (m)	SON (m)	DJF (m)
ARSH	2.144	2.164	2.122	2.139	2.148
DODM	2.204	2.221	2.152	2.173	2.226
KFNY	2.040	2.061	1.980	2.018	2.081
MAL2	2.571	2.600	2.554	2.566	2.565
MBAR	2.167	2.182	2.155	2.170	2.159
MBEY	2.041	2.063	1.983	2.015	2.081
MOIU	1.916	1.921	1.922	1.917	1.893
MTDK	2.386	2.419	2.329	2.361	2.430
MTVE	2.564	2.599	2.501	2.533	2.610
NURK	2.126	2.138	2.101	2.125	2.124
RCMN	2.077	2.083	2.074	2.077	2.069
SNGC	2.187	2.209	2.127	2.168	2.238
TNDC	2.338	2.359	2.277	2.310	2.395

The variability of ZTD depends on season, topography and climatic conditions of the region (Choy et al., 2015). The range of ZTD in East African tropical Region is between 1.9 m and 2.6 m depending on the GNSS site (Table 3). Generally ZTD or ZWD variations exhibited significant seasonal dependence in this study, with larger values in the rainy (wet) season and lower ones in the (dry) season and the same findings were also reported by Isioye et al. (2018). However, further analysis about the seasonal cycle, interannual and intraseasonal variability, as well as diurnal cycle in GPS ZTD data over the East African tropical region is required.

In this study, the dependence of GNSS ZTD and ZWD on station elevation were also examined. It was processed by taking the average goGPS ZTD and ZWD measurements at a particular station and plotting them with the site elevation as shown in Fig. 8. Fig. 8(a) and (b) show a strong negative correlation between ZTD or ZWD and elevation for all stations under study. It has however been shown previously that ZTD or ZWD estimates exhibit strong correlation with station elevation e.g. Isioye et al. (2015a,b). Therefore, the amount of ZTD values decrease with increasing station elevation. For example, stations MAL2 and MTVE located at low elevation (−20.9 m and −11.4 m) have larger average ZTD values as compared to those at high elevation such as MOIU (2201.5 m) among others. This is due to the atmospheric pressure variations with the height increase where low pressure regions have less atmospheric mass above their locations, whereas high pressure areas have more atmospheric mass above their locations. Therefore, as the elevation increases, there are exponentially fewer air molecules (Jin et al., 2007). Furthermore, the higher ZTD or ZWD values at low elevation is probably due to higher evaporation due to the presence of water

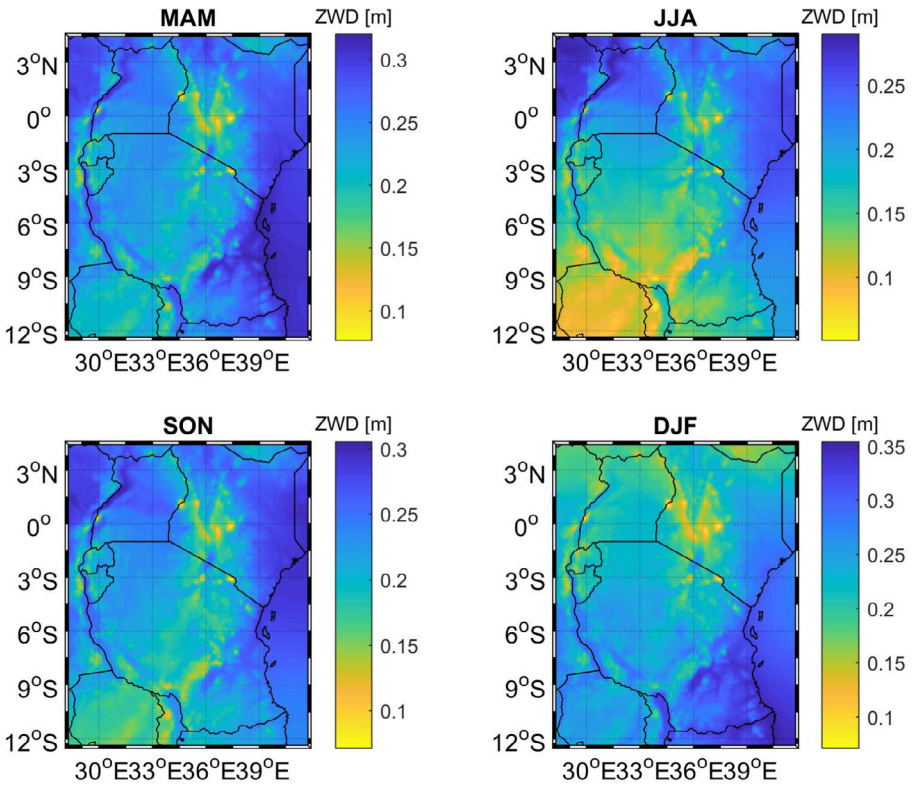

Fig. 7. Spatial and seasonal variations of UEMS NWP ZWD for four seasons over East Africa tropical region.

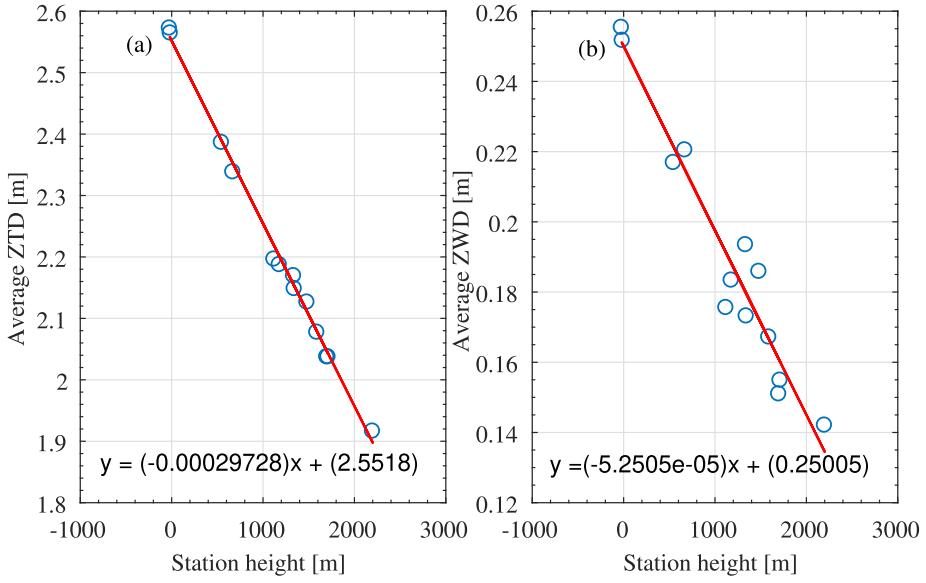

Fig. 8. Plot of average GNSS (a) ZTD and (b) ZWD against station elevation.

vapour, dense vegetation and longer periods of rainfall. Also the ZTD or ZWD dependence on elevation is due to the water vapour which is integrated from the observation station to the top of the troposphere. If the observation station is at a high elevation, it will be exposed to a less troposphere and hence less water vapour above it to delay the GNSS signal since the major source of water vapour is the earth's troposphere (Isioye et al., 2015a).

3.2. Comparison between goGPS and APPS ZTD

Daily mean GNSS data from 13 stations from 2013 to 2016 were processed to represent the distribution of the GNSS sites over the East African tropical region. To assess the accuracy and performance of the ZTD computed from goGPS, the ZTD estimates were compared to the APPS ZTD measurements. For each site, we computed the

average bias (goGPS ZTD – APP ZTD), RMS difference between the ZTDs and standard deviation. The statistical comparison of ZTD estimation between goGPS, and APPS are shown in Table 4. A comparison was made when there was an epoch match between goGPS and APPS ZTD results. Figs. 9 and 10 shows scatter plots of goGPS ZTD versus APPS ZTD for stations in subregion 1 and 2 respectively. In both figures, it can be observed that ZTD estimates from goGPS are consistent to those of APPS with an overall average bias, RMS and standard deviation of −0.9 mm, 3.2 mm and 3.0 mm respectively. This indicates that both software provide estimates of comparable accuracy at a millimeter level. At the individual stations, the bias range between −1.8 mm and 0.0 mm, the RMS between 2.3 mm and 7.7 mm and the standard deviation between 2.1 mm and 7.6 mm for all the 13 stations. The higher RMS and stdev at ARSH of 7.7 and 7.6 m respectively is probably due to the L2 data loss exposing the results to a very active ionosphere over this low latitude area. This was observed after both the goGPS and the APPS software rejected some GPS data files. It was discovered that in the rejected files, L2 data were completely missing and some of the accepted files missed some L2 data. Jiang et al. (2016) discovered that loss of GPS L2 data reduces the accuracy of the GPS ZTD. It is therefore essential to perform quality control for the GPS data files (Jiang et al., 2016) before the GPS ZTD retrieval.

The bias in this study is found to be negative at almost all stations. This indicates that the ZTD estimates from the goGPS are lower than those from APPS, indicating a

Table 4
Summary of correlation, bias, RMS and standard deviation of goGPS ZTD with respect to APPS ZTD at the 13 GPS stations.

Site	Corr	Bias (mm)	RMS (mm)	Stdev (mm)	No. data
ARSH	0.974	−1.6	7.7	7.6	1128
DODM	0.998	−1.8	3.2	2.7	812
KFNY	0.999	−1.2	2.4	2.1	956
MAL2	0.998	−0.6	2.7	2.6	1419
MBAR	0.997	−0.6	2.3	2.2	1169
MBEY	0.998	−1.2	2.9	2.7	804
MOIU	0.995	−0.8	2.8	2.7	1228
MTDK	0.999	0.0	2.6	2.6	1102
MTVE	0.999	−0.3	3.1	3.1	831
NURK	0.969	0.0	3.5	3.5	838
RCMN	0.997	−1.5	2.8	2.4	921
SNGC	0.999	−0.9	2.7	2.6	945
TNDC	0.999	−0.8	2.5	2.4	736
Mean		−0.9	3.2	3.0	

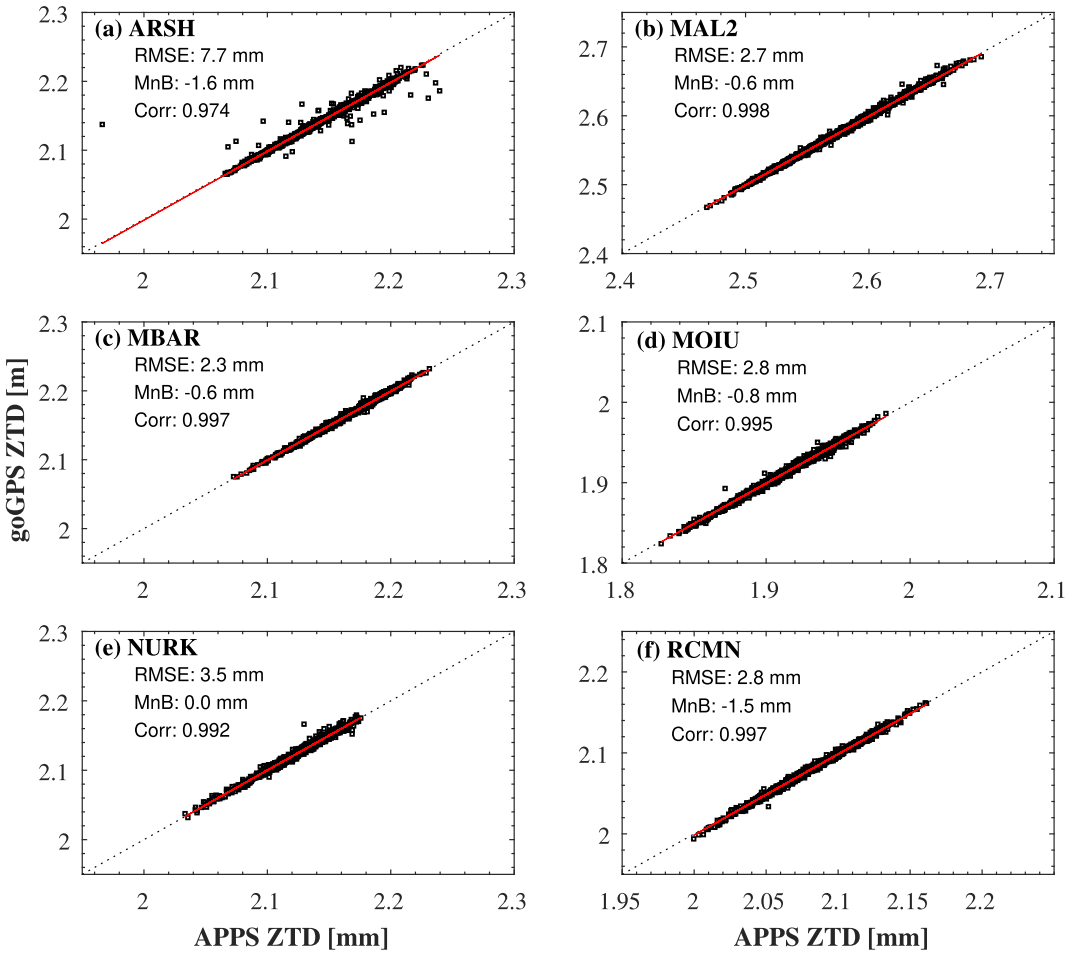

Fig. 9. Scatter plots of goGPS ZTD versus APPS ZTD for stations in subregion 1.

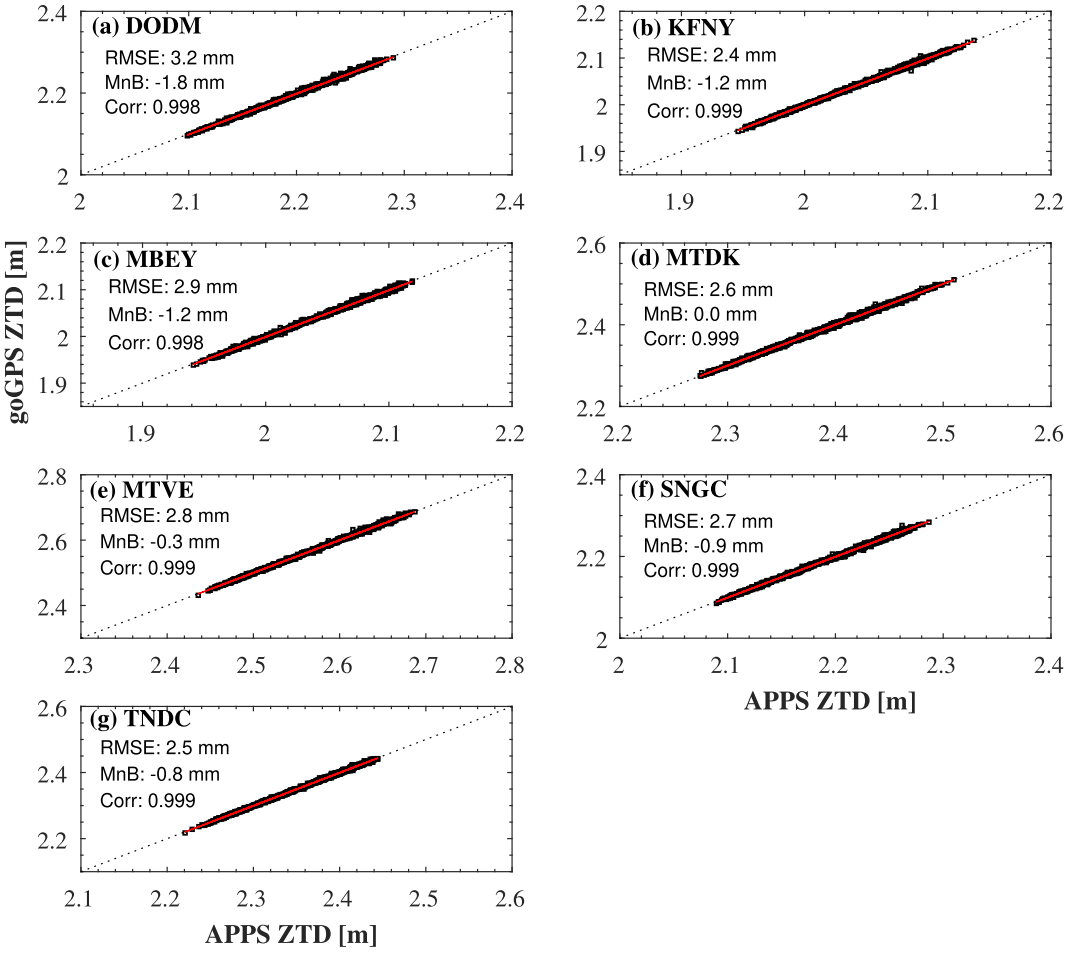

Fig. 10. Scatter plots of goGPS ZTD versus APPS ZTD for stations in subregion 2.

general underestimation of ZTD by the goGPS. The corresponding linear correlations between the goGPS and the APPS ZTDs at all stations are also illustrated in Figs. 9 and 10, and Table 4. The ZTDs from the two software are highly correlated, with the correlation coefficients ranging between 0.969 and 0.999.

Krietemeyer et al. (2018) reported that the difference between the goGPS ZTD and that from the IGS reference ZTD dataset shows the biases and RMS range of 2.6–9.0 mm and 7.2–15.8 mm respectively. Based on over two years of data, Haase et al. (2003) reported that the difference between radiosonde and GPS ZTD has a standard deviation of 12 mm of delay and a bias of 7 mm of delay. Comparing with the results in this study, the accuracy of the estimated ZTD has been improved. This could probably be due to the application of a newer version of the goGPS with improved mapping function (VMF).

The RMS of the different stations as presented in Table 4 were plotted against the latitude to ascertain the influence of the latter on the corresponding RMS. From Fig. 11 it is evident that no clear relationship exists between the RMS and station latitudes. The results in this study however, do not match with those reported by others such as Lu et al. (2016) and Astudillo et al. (2018). Therefore, the study on the quality of ZTD estimation at different latitudes needs to be further confirmed with much denser GPS network in the future.

3.3. GNSS and NWP ZTD comparison

GNSS data from eight stations out of 13 stations from June 2015 to May 2016 from the East African tropical region were selected for comparison with the numerical weather prediction model. The selection of the stations and the period was based on the availability of data and on the regional distribution of the stations over the study area. To validate the accuracy and performance of the ZTD computed from goGPS, the estimates were compared to the UEMS NWP ZTD measurements. For each of the eight sites, we compute average bias (goGPS ZTD – NWP ZTD), RMS difference between the ZTDs and standard deviation. A statistical comparison between the GNSS (goGPS) and UEMS NWP ZTD for the selected stations is presented in Table 5. Fig. 12 shows scatter plots of daily mean GNSS ZTD versus NWP ZTD at the selected stations. From Fig. 12 and Table 5, the bias values

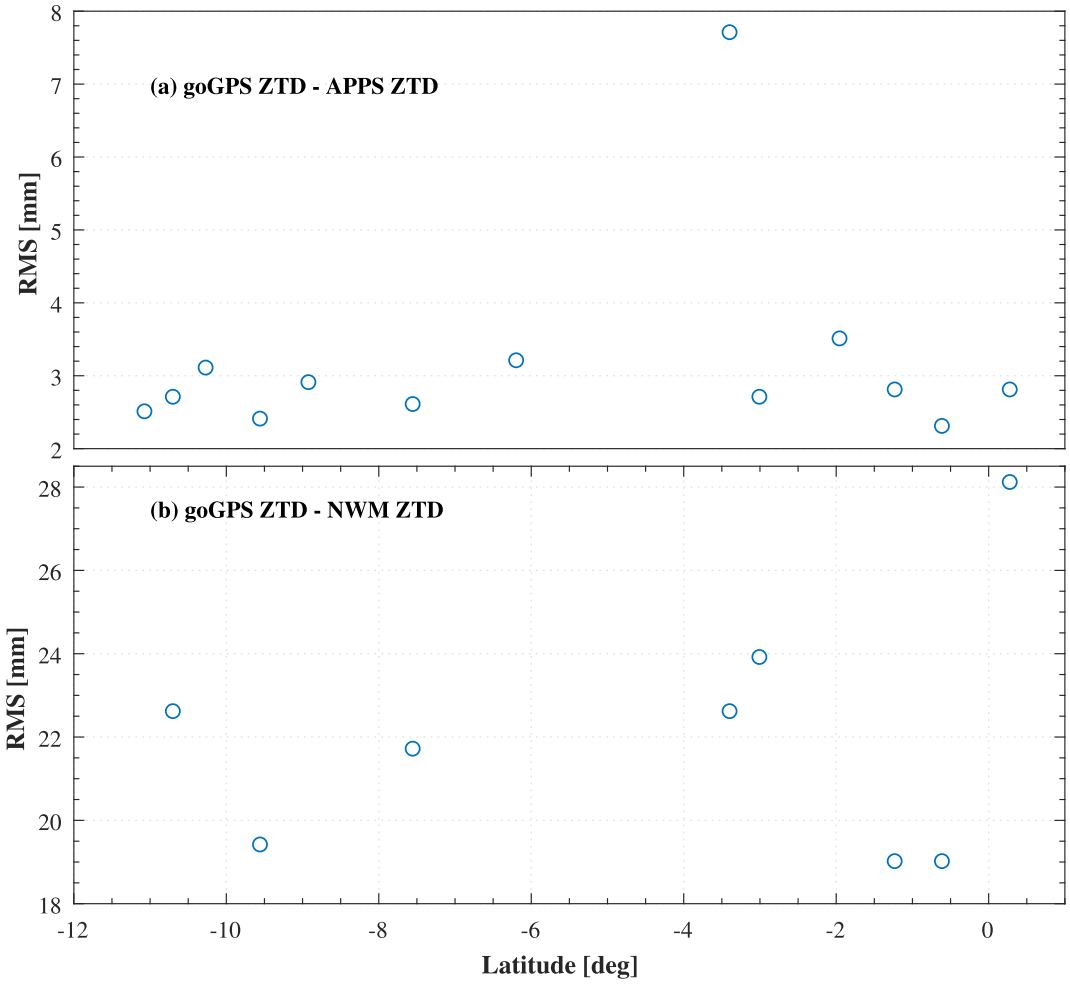

Fig. 11. RMS of ZTD from goGPS compared with (a) APPS and (b) NWP.

at individual stations between UEMS NWP and GPS ZTD, are in the range −22.1 mm to −5.2 mm with an overall average bias of −12.4 mm. The RMS values are in the range 19.0–28.1 mm with an overall average of 22.0 mm and stdev values are in the range 14.0–20.7 mm with an overall average of 17.6 mm. The high ZTD bias and RMS between UEMS NWP and GPS measurements at MOIU is probably due to altitude extrapolation errors. The graphs in Fig. 12, further demonstrate that the two datasets highly correlate, with correlation coefficients ranging between 0.802 and 0.974. However, stations from subregion 1 have low correlation coefficients (0.802–0.875) as compared to stations in subregion 2 (0.956–0.974). The smaller correlation at equatorial sites is probably due to the smaller seasonal cycle at these sites (Bock et al., 2007). The negative bias at all stations indicates that the ZTD estimates from the NWP are higher than those from GNSS (goGPS), indicating a general overestimation of ZTD by the NWP in this region.

Table 5
Summary of correlation, bias, RMS and standard deviation of GOGPS ZTD compared to UEMS NWP ZTD.

Site	Corr	Bias (mm)	RMS (mm)	Stdev (mm)	No. data
ARSH	0.802	−9.1	22.6	20.7	257
KFNY	0.974	−13.5	19.4	14.0	332
MAL2	0.875	−15.0	23.9	18.6	328
MBAR	0.842	−5.2	19.0	18.3	142
MOIU	0.825	−22.1	28.1	17.4	261
MTDK	0.956	−11.1	21.7	18.7	331
RCMN	0.842	−6.4	19.0	17.9	287
SNGC	0.967	−16.8	22.6	15.1	198
Mean		−12.4	22.0	17.6	

Several studies have reported about the performance of GPS ZTD as compared to the NWP model. For example, Haase et al. (2003) reported that the standard deviation between the GPS ZTD and High-Resolution Limited-Area Model (HIRLAM) NWP model is about 18 mm. Lu et al. (2016) reported that the mean biases between the ECMWF and IGS ZTDs are within ±15 mm, while the rms values of the ZTD differences are less than 22 mm. Akilan et al. (2015) also reported that the GPS data from two IGS GPS stations located in the equatorial Indian Ocean region were processed and the ZTD values were compared with the NWM ZTD values. The standard deviations obtained are 28 mm and 17 mm at the sites

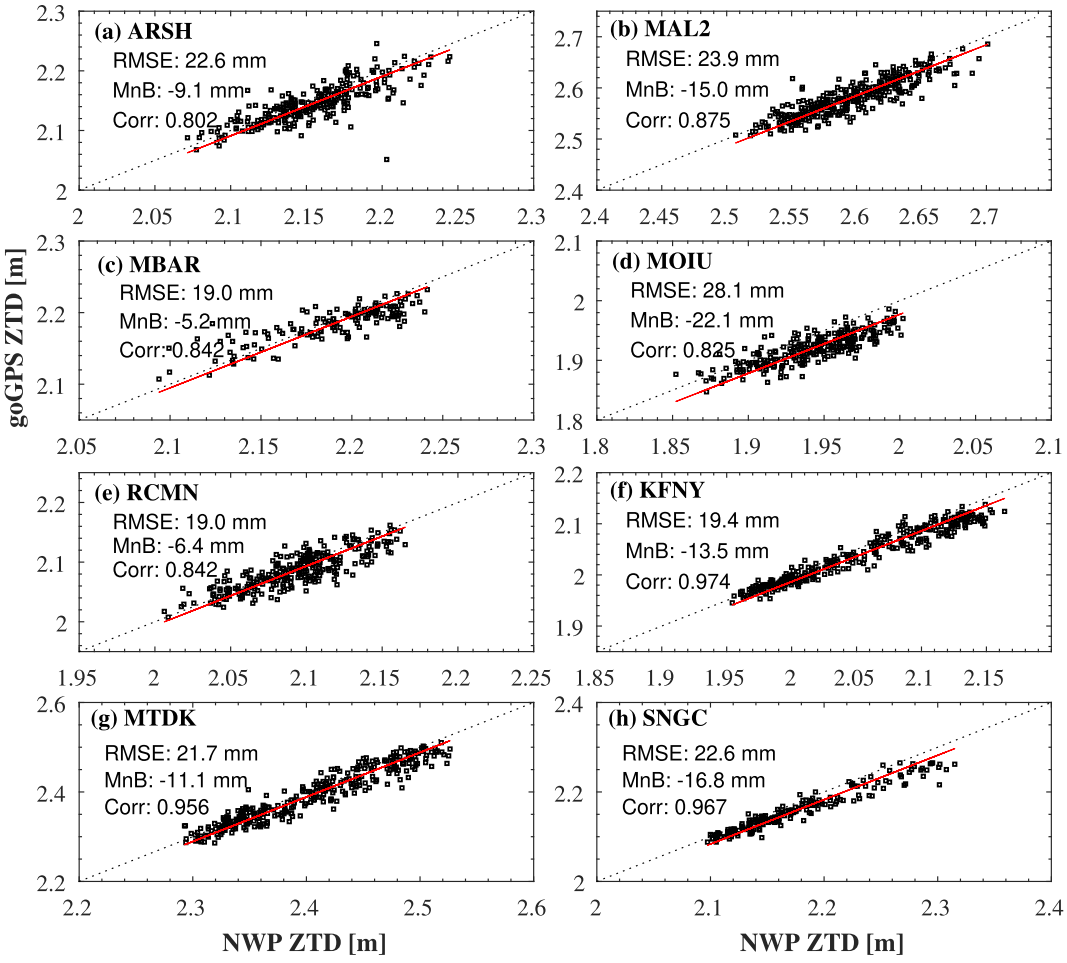

Fig. 12. Scatter plots of goGPS ZTD versus NWP ZTD with (a)–(e) representing station in subregion 1 and (f)–(h) representing stations in subregion 2.

respectively. Wonnacott and Merry (2006) reported that for Poland, the ZTD data set based on meteorological parameters from the NWP WRF model and from a combination of the NWP model and GNSS ZTDs shows an average standard deviation of 17.0 mm with respect to the reference GNSS stations. The biases, RMS and stdev values from the comparison of UEMS NWP and the GPS ZTD data in this study are in agreement with previous mentioned studies. However, many factors should also be considered in this comparison such as difference in topography, GPS network density, difference in the skills of the different NWP model over different regions.

The application of ZTD estimates in NWP nowcasting and monitoring extreme short-term weather changes, requires an accuracy of 5–30 mm (Offiler, 2010) as cited by Ahmed et al. (2016). According to Ahmed et al. (2016), the requirements for NWP nowcasting were revised during the new COST Action ES1206 (GNSS4SWEC). Therefore, accuracy requirements for ZTD applied in this study, are 6 mm (0.6 cm) target and 30 mm (3 cm) threshold values as presented by Ahmed et al. (2016). Considering the RMS as a measure of relative accuracy, the obtained goGPS – NWP ZTD software can be compared with these requirements as explained by Ahmed et al. (2016). It can be seen from Table 5, that all stations considered in this study, meet the threshold requirement for relative accuracy. Therefore, the agreement between the GPS ZTD and the NWP ZTD demonstrates the acceptable accuracy and indicates that GPS ZTD from the East African tropical region can be assimilated into NWP models.

Fig. 13 presents the monthly mean ZTD variability from GPS and UEMS NWP model for subregions 1, (a)–(e) and subregion 2, (f)–(h) from June 2015 to May 2016. From stations (a)–(e), the ZTD values are maximum at most GPS sites in April and November while stations (f)-(h), show maximum values in January and April. It is observed that the seasonal cycle of the ZTD has a bimodal pattern for stations in subregion 1 with high ZTD in spring season (MAM) while subregion 2 shows a mono modal type ZTD content with the high ZTD in summer season (DJF). For the two subregions, the ZTD values show peaks in the rainy season. According to Mengistu et al. (2015), the cause of this ZTD season cycle could be due the role of local features, such as the proximity to moisture sources.

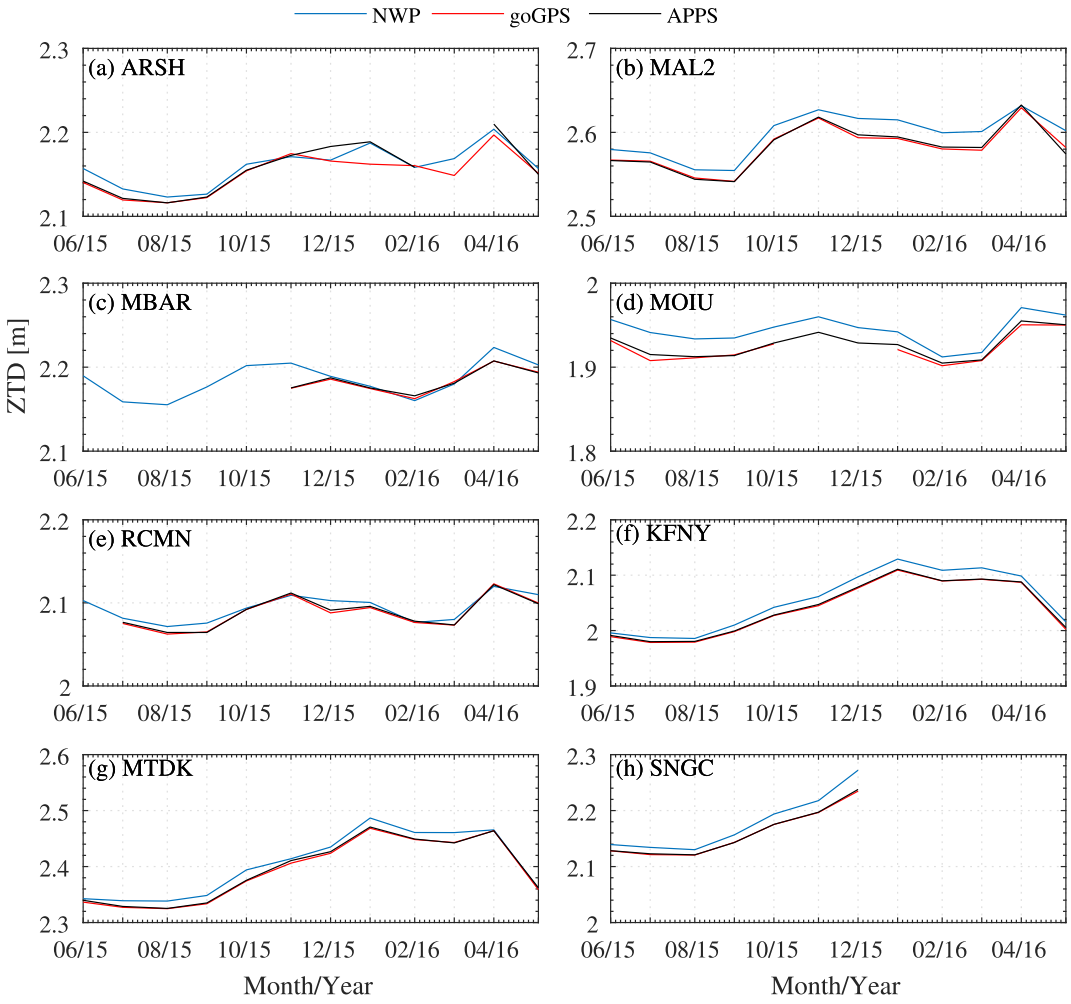

Fig. 13. Comparison of monthly mean ZTD time series from goGPS, APPS, and UEMS NWP data. Stations (a)–(e) are from subregion 1 and stations (f)–(h) are from subregion 2.

4. Conclusion

In this study the ZTD time series (2013–2016) with a resolution of 1 h at 13 sites over East African tropical region are obtained and analyzed. In order to investigate the oscillations that describe the annual variation of the ZTD time series, the Lomb Scargle periodograms were calculated from the time series. It was discovered that the semi-annual frequency has the dominant power for stations in subregion 1, the region nearest to the equator and the annual frequency has the dominant power for stations in subregion 2. However further study is required to use the discovered annual and semi-annual term to describe more the seasonal variations, including amplitude and phase shift in East African tropical region. Also further study is required to estimate the linear trend from the ZTD time series. In this study this was not considered due to the gaps in the ZTD time series data.

The goGPS, APPS software and the UEMS model were applied in this study and the discrepancies between the datasets are analysed. The comparison between goGPS and APPS ZTD at the 13 stations shows a mean bias, RMS and standard deviation ranging between −1.8 mm to 0.0 mm, 2.3 mm to 7.7 mm and 2.1 mm to 7.6 mm respectively. This gives an overall average bias, RMS and standard deviation at all the 13 stations as −0.9 mm, 3.2 mm and 3.0 mm respectively. The higher RMS and stdev at ARSH of 7.7 and 7.6 m respectively is probably due to the L2 data loss exposing the results to a very active ionosphere over this low latitude area. However comparing our study with previous studies, the ZTD accuracy has been improved. The study however, shows variations in the magnitude of bias of goGPS ZTD with respect to APPS ZTD without clear pattern from station to station. The causes of variations in bias at different stations may be due to availability and quality of the GPS data. The goGPS ZTD showed a good correlation with the APPS ZTD values at all the stations with correlation coefficients ranging between 0.969 and 0.999.

The ZTD estimates derived from goGPS (GNSS) and the ZTD values obtained from the UEMS (NWP) were also analyzed for the period of a year (June 2015 to May 2016). The GPS ZTD showed a good correlation with the NWP ZTD values. The correlation between the two

datasets ranges between 0.802 and 0.974 at the eight stations, with a mean bias, RMS and standard deviation ranging between −22.1 mm to −6.4 mm, 19.0 mm to 28.1 mm and 14.0 mm to 20.7 mm respectively. This comparison gave an overall average bias, RMS and standard deviation of −12.4 mm, 22.0 mm and 17.6 mm respectively at the 8 stations. The comparison of UEMS NWP and the GPS ZTD data in this study is in agreement with previous studies. Following Ahmed et al. (2016), it was discovered that GPS ZTD in the East Afican tropical region meet the accuracy requirements for assimilation into NWP models.

In this study, it was observed that average values of ZTD ranges from 1.9 m to 2.6 m depending on the site. The lower ZTD and ZWD values are located at the areas of higher altitude and the higher ZTD and ZWD values are concentrated at stations located at lower altitudes. The cause of high ZTD values at low altitude is due to very high temperature and their proximity to the Indian Ocean. Generally, the mean ZTD decreases with increasing altitude due to the atmospheric pressure decrease with the height increase. For subregions 1 and 2 considered in this study, larger average ZTD and ZWD values are observed during the spring and summer season while lower average ZTD values are observed during summer and winter seasons respectively.

Acknowledgments

The research project was partly funded by the European Union's Horizon 2020 research and innovation programme under grant agreement No. 776691 (TWIGA). R.C. Ssenyunzi acknowledges the financial support from Busitema University.

References

Abdelfatah, M.A., Mousa, A.E., Salama, I.M., El-Fiky, G.S., 2009. Assessment of tropospheric delay models in GPS baseline data analysis: a case study of a regional network at upper Egypt. J. Civil. Eng. Res. Mag. AL-Azhar Univ. 31 (4), 1143–1156.

Abdelfatah, M.A., Mousa, A.E., El-Fiky, G.S., 2015. Precise troposphere delay model for Egypt, as derived from radiosonde data. J. Astron. Geoph. 4, 16–24.

Abraha, K.E., Lewi, E., Masson, F., Boy, J., 2015. Spatial-temporal variations of water vapor content over Ethiopia: a study using GPS observations and the ECMWF model. GPS Solut.

Adegoke, A., Onasanya, M., 2008. Effect of propagation delay on signal transmission. Pacific J. Sci. Technol. 9, 13–19.

Ahmed, F., Vaclavovic, P., Teferle, F.N., Dousa, J., Bingley, R., Laurichesse, D., 2016. Comparative analysis of real-time precise point positioning zenith total delay estimates. GPS Solut. 20, 187–199.

Aigong, X., Zongqiu, X., Maorong, G., Xinchao, X., Huizhong, Z., Xin, S., 2013. Estimating zenith tropospheric 5 delays from BeiDou navigation satellite system observations. Sensors 13, 4514–4526.

Akilan, A., Azeez, K.K., Balaji, S., Schuh, H., Srinivas, Y., 2015. GPS derived Zenith Total Delay (ZTD) observed at tropical locations in South India during atmospheric storms and depressions. J. Atmosp. Solar-Terrest. Phys. 125–126, 1–7.

Anyah, R.O., Semazzi, F.H., Xie, L., 2006. Simulated physical mechanisms associated with climate variability over Lake Victoria Basin in East Africa. Month. Weath. Rev. 134, 3588–3609.

Astudillo, J.M., Lau, L., Tang, Y., Moore, T., 2018. Analysing the Zenith Tropospheric Delay Estimates in On-line Precise Point Positioning (PPP) Services and PPP Software Packages. Sensors. pp. 1–6.

Baby, H.B., Gole, P., Laverbnat, J., 1988. A model for the tropospheric excess path length of radio waves from surface meteorological measurements. Radio Sci. 23, 1023–1038.

Barindelli, S., Realini, E., Venuti, G., Fermi, A., Gatti, A., 2018. Detection of water vapor time variations associated with heavy rain in northern Italy by geodetic and low-cost GNSS receivers. Earth Planet. Space 70 (1), 28.

Bhattacharya, S., Dubey, S., Tiwari, R., Purohit, P.K., Gwal, A.K., 2008. Effect of magnetic activity on ionospheric time delay at low latitude. J. Astrophys. Astr. 29, 269–274.

Bock, O., Nuret, M., 2009. Verification of NWP model analyses and radiosonde humidity data with GPS precipitable water vapor estimates during AMMA. Weather Forecast. 24 (4), 1085–1101.

Bock, O., Keil, C., Richard, E., Flamant, C., Bouin, M.N., 2005. Validation of precipitable water from ECMWF model analyses with GPS and radiosonde data during the MAP SOP. Q.J. Roy. Meteor. Soc. 131, 3013–3036.

Bock, O., Bouin, M.N., Walpersdorf, A., Lafore, J.P., Janicot, S., Guichard, F., A, A.P., 2007. Comparison of ground-based GPS precipitable water vapor to independent observations and NWP model reanalyses over Africa. Q.J.R. Meteorol. Soc. 133, 2011–2027.

Böhm, J., Niell, A., Tregoning, P., Schuh, H., 2006. Global mapping function (GMF): a new empirical mapping function based on numerical weather model data. J. Geophys. Res. Lett. 33.

Brenot, H., Ducrocq, V., Walpersdorf, A., Champollion, C., Caumont, O., 2006. GPS zenith delay sensitivity evaluated from high-resolution numerical weather prediction simulations of the 8–9 September 2002 flash flood over southeastern France. J. Geophys. Res. 111 (D15), D15105.

Camberlin, P., 1997. Rainfall anomalies in the source region of the Nile and their connection with the Indian summer monsoon. J. Clim. 10, 1380–1392.

Camberlin, P., 2018. Oxford Research Encyclopedia of Climate Science. climatescience.oxfordre.com.

Choy, S., Wang, C., Yeh, T., Dawson, J., Jia, M., Kuleshov, Y., 2015. Precipitable water vapor estimates in the Australian Region from ground-based GPS observations. Adv. Meteorol. https://doi.org/10.1155/2015/956481.

Davies, T.D., Vincent, C.E., Beresford, A.K.C., 1985. July-August rainfall in West-Central Kenya. J. Clim. 5, 17–33.

Davis, J.L., Herring, T.A., Shapiro, I.I., Rogers, A.E.E., Elgered, G., 1985. Geodesy by radio interferometry: effects of atmospheric modeling on estimates of baseline length. Radio Sci. 20, 1593–1607.

Dodo, J.D., Idowu, T.O., 2010. Regional assessment of the GPS tropospheric delay models on the African GNSS network. J. Emerg. Tren. Engin. Appl. Sci. 1, 113–121.

Dousa, J., Vaclavovic, P., 2014. Real-time zenith tropospheric delays in support of numerical weather prediction applications. Adv. Space Res. 53 (9), 1347–1358.

Emardson, T.R., Elegered, T.R., Johansson, J.M., 1998. Three months of continuous monitoring of atmospheric water vapor with a network of global positioning system receivers. J. Geophys. Res. 03, 1807–1820. https://doi.org/10.1029/97JD03015.

Endris, H., Omondi, P., Jain, S., Lennard, C., Hewiston, B., Chang'a, L., Awange, J., Dosio, A., Ketiem, P., Nikulin, G., Panitz, H., Buchner, M., Stordal, F., Tazalika, L., 2013. Assessment of the performance of CORDEX regional climate models in simulating East African Rainfall. J. Clim. 26, 8453–8475.

Favre, A., Stone, D., Cerezo, D., Philippon, N., and Abiodun, B., 2011. Diagnostic of monthly rainfall from CORDEX simulations over Africa: Focus on the annual cycles. In: On the Coordinated Regional

Climate Downscaling Experiment-CORDEX. Trieste, Italy, World Climate Research Program, Proc. Int. Conf.
Glynn, E.F., Chen, J., Mushegian, A.R., 2006. Detecting periodic patterns in unevenly spaced gene expression time series using Lomb-Scargle periodograms. Bioinformatics 22 (3), 310–316.
Guerova, G., Jones, J., Dousa, J., Dick, G., de Haan, S., Pottiaux, E., Bock, O., Pacione, R., Elgered, G., Vedel, H., Bender, M., 2016. Review of the state of the art and future prospects of the ground-based GNSS meteorology in Europe. Atmos. Meas. Tech. 9, 5385–5406.
Haase, J., Ge, M., Vedel, H., Calais, E., 2003. Accuracy and variability of GPS tropospheric delay measurements of water vapor in the western Mediterranean. J. Appl. Meteorol. 42, 1547–1568.
Hackman, C., Guerova, G., Byram, S., Dousa, J., Hugentobler, U., 2015. International GNSS Service (IGS) Troposphere Products and Working Group Activities.
Hadas, T., Kaplon, J., Bosy, J., Sierny, J., Wilgan, K., 2013. Near real-time regional troposphere models for the GNSS precise point positioning technique. Meas. Sci. Technol. 24 (5), 055003.
Herrera, M.A., Suhandri, H.F., Realini, E., Reguzzoni, M., Clara de Lacy, M., 2016. gogps: open-source matlab software. GPS Solut. 20 (3), 595–603.
Hocke, K., Kämpfer, N., 2008. Gap filling and noise reduction of unevenly sampled data by means of the Lomb-Scargle periodogram. Atmos. Chem. Phys. Discuss. 8, 4603–4623.
Isioye, O.A., Combrinck, L., Botai, O.J., Munghemezulu, C., 2015a. The potential for observing AfricanWeather with GNSS. Adv. Meteorol., 1–16
Isioye, O.A., Combrinck, L., Botai, J., 2015b. Performance evaluation of blind tropospheric delay correction models over Africa. South African J. Geom. 4 (4), 502–525.
Isioye, O.A., Combrinck, L., Botai, J., 2018. Evaluation of spatial and temporal characteristics of GNSS-derived ZTD estimates in Nigeria. Theor. Appl. Climatol. 132, 1099–1116.
Jiang, P., Ye, S., Chen, D., Liu, Y., Xia, P., 2016. Retrieving precipitable water vapor data using GPS zenith delays and global reanalysis data in China. Remote Sens. 8, 396.
Jin, S., Park, P., 2005. A new precision improvement of zenith tropospheric delay estimates by GPS. Curr. Sci. 89, 997–1000.
Jin, S., Park, J., Cho, J., Park, P., 2007. Seasonal variability of GPS-derived zenith tropospheric delay (1994–2006) and climate implications. J. Geophys. Res. 112, 1–11.
Jin, S., Luo, O.F., Gleason, S., 2009. Characterization of diurnal cycles in ZTD from a decade of global GPS observations. J. Geod. 83, 537–545. https://doi.org/10.1007/s00190-008-0264-3.
Klos, A., Hunegnaw, A., Teferle, F.N., Abraha, K.E., Ahmed, F., Bogusz, J., 2018. Statistical significance of trends in Zenith Wet Delay from re-processed GPS solutions. GPS Solut. 22 (51). https://doi.org/10.1007/s10291-10018-10717-y.
Kouba, J., 2008. Implementation and testing of the gridded Vienna Mapping Function 1 (VMF1). J. Geod. 82 (4–5), 193–205.
Kouba, J., 2009. A Guide to Using International GNSS Service (IGS) Products.
Koulali, A., Ouazar, D., Bock, O., Fadil, A., 2011. Study of seasonal scale atmospheric water cycle with ground-based GPS receivers, radiosondes and NWP models over Morocco. Atmos. Res. 41 (104–105), 273–291.
Krietemeyer, A., Veldhuis, M., Marel, V., Realini, E., Giesen, N., 2018. Potential of cost-efficient single frequency GNSS receivers for water vapor monitoring. Rem. Sens. 10 (9), 1493.
Kurekar, R., Kuraishi, M., 2012. Determination of precipitable water vapor using global positioning system. Int. J. Geol. Earth Environ. Sci. 2, 51–57.
Lomb, N., 1976. Least-squares frequency analysis of unequally spaced data. Space Sci. 39, 448–462.
Lou, Y., Huang, J., Zhang, W., Liang, H., Zheng, F., Liu, J., 2018. A New Zenith Tropospheric Delay Grid Product for Real-Time PPP Applications Over China. Sensors. pp. 1–14.
Lu, C., Zus, F., Ge, M., Heinkelmann, R., Dick, G., Wickert, J., Schuh, H., 2016. Tropospheric delay parameters from numerical weather models for multi-GNSS precise positioning. Atmos. Meas. Tech. 9, 5965–5973.
Mengistu, T., Blumenstock, T., Hase, F., 2015. Observations of precipitable water vapour over complex topography of Ethiopia from groundbased GPS, FTIR, radiosonde and ERA-Interim reanalysis. Atmos. Meas. Tech. 8, 3277–3295.
Mousa, A.E., 2012. Temporal and spatial variation of the zenith tropospheric delay: case study of egyptian territory. Mar. Sci. 23 (2), 97–108.
Musa, T.A., Musa, N., Amir, S., Othman, R., Ses, S., Omar, K., Abdullah, K., Lim, S., Rizos, C., 2011. GPS meteorology in a low latitude region: remote sensing of atmospheric water vapor over the Malaysian Peninsula. J. Atmosp. Solar-Terrest. Phys. 73, 2410–2422.
Mutai, C.C., Ward, M.N., Colman, A.W., 1998. Towards the prediction of the east Africa short rains based on sea-surface temperature atmosphere coupling. Int. J. Climatol. 18, 975–997.
Nicholson, S.E., 1996. A review of climate dynamics and climate variability in Eastern Africa. In: Johnson, T.C., Odada, E.O. (Eds.), The Limnology, Climatology, and Paleoclimatology of the East African lakes. pp. 25–56.
Niell, A.E., 1996. Global mapping functions for the atmospheric delay at radio wavelengths. J. Geophys. Res. 111, 3227–3246.
Niell, A.E., 2000. Improved atmospheric mapping functions for VLBI and GPS. Earth Plant. Space 52 (10), 699–702.
Notarpietro, R., Cucca, M., Bonafoni, S., 2012. GNSS Signals: A Powerful Source for Atmosphere and Earth's Surface Monitoring. Yann Chemin (for InTech).
Offiler, D., 2010. Product requirements document version 1.0-21 December 2010. EIG EUMETNET GNSS Water Vapour Programme (E-GVAP-II).
Realini, E., Reguzzoni, M., 2013. gogps: open source software for enhancing the accuracy of low-cost receivers by single frequency relative kinematic positioning. Meas. Sci. Technol. 24 (11), 115010.
Rueger, J., 2002. Refractive Indices of Light, Infrared and Radio Waves in the Atmosphere, Sydney, Australia: School of Surveying and Spatial Information Systems. University of New South Wales.
Saastamoinen, J., 1972. Atmospheric correction for the troposphere and stratosphere in radio ranging of satellites, Geophysical Monogram Series. American Geophysical Union, Band 15, Washington, D.C., pp. 247–251.
Schuler, T., 2001. On ground-based GPS tropospheric delay estimation, Ph.D. thesis. Institute of Geodesy and Navigation, University FAF, Munich, 25 Germany.
Solheim, S., Vivekanandan, J., Ware, H., Rocken, C., 1999. Propagation delays induced in GPS signals by dry air water vapor hydrometeors and other particulates. J. Geophys. Res. 104, 9663–9670.
Song, S., Zhu, W., Chen, Q., Liou, Y., 2011. Establishment of a new tropospheric delay correction model over China area. Sci. China. Phys. Mech. Astron. 54, 2271–2283.
Teke, K., Boehm, J., Nilsson, T., Schuh, H., Steigeberger, P., Dach, P., Heinkelman, R., Willis, P., Haas, R., Garcia-Espada, S., Hobiger, T., Pchikawa, R., Shimizu, S., 2011. Multi-technique comparison of troposphere zenith delays and gradients during CONT08. J. Geod. 85 (7), 395–493. https://doi.org/10.1007/s00190-010-0434-y.
Valadez, M.D., Corcard, M., Santerre, R., 2007. 3D modelling of the tropospheric refractivity using permanent GPS network. Geomatica 61, 445–453.
Vedel, H., Mogensen, K.S., Huang, X., 2001. Calculation of zenith delay from meteorological data: comparison of NWP model, radiosondes and GPS delay. Phys. Chem. Earth. 26, 497–502.
Walpersdorf, A., Bouin, M.N., Bock, O., Doerflinger, E., 2007. Assessment of GPS data for meteorological applications over Africa: study of error sources and analysis of positioning accuracy. J. Atmos. Solar-Terrest. Phys. 69 (12), 1312–1330.
Wilgan, K., Hurter, F., Geiger, A., Rohm, W., Bosy, J., 2017. Tropospheric refractivity and zenith path delays from least-squares

collocation of meteorological and GNSS data. Review 38 (301), 594–607.
Wonnacott, R.T., Merry, C.L., 2006. The use of GPS for the estimation of precipitable water vapor for weather forecasting and monitoring in South Africa. J. Geod. 91, 117–134.
Yang, W., Seager, R., Cane, M.A., Lyon, B., 2015. The annual cycle of east African precipitation. J. Clim. 28, 2385–2404.
Yao, Y., Zhang, B., Xu, C.Q., He, C., Yu, C., Yan, F., 2016. A global empirical model for estimating zenith tropospheric delay. Sci. China Earth. 59, 118–128.
Younes, S.A., 2016. Modeling investigation of wet tropospheric delay error and precipitable water vapor content in Egypt. Egypt. J. Remot. Sens. Space Sci. 19, 333–342.
Zechmeister, M., Kurster, M., 2009. The generalised Lomb-Scargle periodogram a new formalism for the floating-mean and Keplerian periodograms. Astron. Astophy. 496, 577–584.
Zumberge, J.F., Heflin, M.B., Jefferson, D.C., Watkins, M.M., Webb, F. H., 1997. Precise point positioning for the efficient and robust analysis of GPS data from large networks. J. Geophys. Res. 102, 5005–5017.